Imaging of barely visible impact damage on a complex composite stiffened panel using a nonlinear ultrasound stimulated thermography approach

Gian Piero Malfense Fierro, Dmitri Ginzburg, Francesco Ciampa and Michele Meo

University of Bath, Materials Research, Department of Mechanical Engineering, Claverton Down, Bath, UK

Abstract

Thermosonics, also known as ultrasonic stimulated thermography, is a rapid non-destructive evaluation technique that uses an infrared camera to visualise material defects by detecting the frictional heating at crack surfaces when a part under inspection is vibrated. These vibrations are usually produced by an ultrasonic horn being pressed against the surface of the test sample, which result in uncontrolled generations of frequency components and excitation amplitude. This makes thermosonics highly non-reproducible and unreliable. This paper presents a novel thermographic method, here named as nonlinear ultrasound stimulated thermography (NUST), for the detection and imaging of real material defects such as impact damage on a complex composite stiffener panel. This technique combines nonlinear ultrasonic techniques with thermography. A nonlinear ultrasonic approach was used as signature for a reliable frequency-selective excitation of material defects, while an infrared camera was employed to reveal the damage location and severity. A nonlinear narrow sweep excitation method (NNSM) was employed to efficiently excite the local resonance frequencies of the damaged region in order to give rise to the highest nonlinear harmonic response in the material leading to a high heat generation at the crack surface. The experimental tests were carried out with a laser vibrometer in order to better understand the interaction of elastic waves with nonlinear scattering. An *ad-hoc* nonlinear thermal-structural finite element and crack model was developed to study the heat generation caused by the movement of the crack surfaces when elastic waves with a particular frequency impinges on the crack interphase with good agreement with the experimental results. The proposed new method allows to detect single and multiple barely visible impact damage in a quick, reliable and reproducible manner and overcomes the main limitations of classical thermosonics.

Keywords: Thermosonics, Thermography, Nonlinear Ultrasound, BVID, Laser Vibrometer

1.1. Introduction

The ever increasing use of carbon fibre reinforced plastic (CFRP) composite materials across a wide range of engineering fields has led to greater focus on the determination of the presence and location of defects in these materials. The assessment of composites becomes difficult under low velocity impact damage as there may be very little surface flaws but large areas of delamination may occur under the surface which can significantly reduce the materials strength. This type of damage is generally referred to as barely visible impact damage (BVID), and it can be caused during manufacturing as well as in service. Due to the hidden nature of BVID, composite materials must be regularly inspected, furthermore due to the ever increasing size of these structures inspection should be quick and cover large areas. There is significant interest within industry for non-destructive evaluation (NDE) systems due to their ability to rapidly and accurately detect cracks and other defects in structures [1]. Thermosonics relies on the excitation of a medium using a piezoelectric transducer (PZT) or a welding horn and the damage evaluation is obtained by measuring the thermal response with an infrared (IR) camera [2]. One of the biggest issues facing sonic thermography is repeatability due to the physics governing the heat generation process in vibrating defects. It has been shown that heat generation is increased when exciting at certain resonance frequencies [3] but the determination of these frequencies is difficult and repeatability low. Other studies have shown that certain excitation frequencies may in fact terminate heat generation at the crack or damage interface due to an increase

of compressive stresses which lock the interface with static friction [4]. Experimental evidence has shown that heat generation in damage regions can be due to three mechanisms: (i) frictional rubbing of contact regions of damage interfaces, (ii) plastic deformations during crack or damage growth which generate heat in the plastic zone surrounding these areas, and (iii) viscoelastic losses can generate significant heat in some materials and these losses are larger in regions of stress concentration (around delaminations and other defects) [5, 6]. Favro et al. [7-9] used pulsed ultrasonic (20-40 kHz) excitation by means of ultrasonic welding gun along with IR camera in order to image surface and subsurface defects in metals and composites based on the localised frictional heating at the defect location. While this approach yielded relatively good results in detecting surface defects such as fatigue cracks, it performed poorly in terms of probability of detection and repeatability of results when applied to typical defect types in carbon/epoxy composites.

The method presented in this work relies on the frequency excitation of damaged regions, where the excitation frequencies are determined by using fundamental principles of nonlinear ultrasound techniques. The excitation frequencies are considered to be damage-specific resonance frequencies also known as local defect resonance (LDR) which excite and heat the damaged regions [10]. The process identifies the damage specific excitation frequencies which should result in defects (cracks, delaminations) clapping/rubbing together thus generating heat that can be observed using an infrared (IR) camera. It has been experimentally shown that in order to attain the maximum acoustic wave-defect interaction the concept of local defect resonance should be used [11]. Using this concept, a strong wave-defect interaction has been confirmed by a resonance induced rise of local temperature of the defect. The resonance behaviour of horizontal near-surface delamination has also been shown to be dependent on the resonance of the material layer above the defect (thickness D). Thus the first resonance of a delamination can be explained by [12]:

$$f_0 \cong \frac{3.2D}{2a^2}\sqrt{\frac{E}{12\rho(1-\sigma^2)}}, \quad (1)$$

where a is the radius, E is the Young's Modulus, ρ is the density of the material and σ is Poisson's ratio. In reality, with unknown damage, determination of the LDR becomes difficult. Further adding to the difficulty in finding the LDR is the complexity of composite failure modes and composite structure shapes (such as a curved stiffener panel). In this paper, phased array analysis of various impact damage shows that delamination occurs throughout the thickness (D), and that the size (a) at each layer varies, as is expected with BVID. Thus an experimental methodology is outlined which does not require the determination of the LDR, but rather requires the repeated sweep excitation over a narrow frequency band of the stiffener panel. This excitation methodology results in the excitation of multiple LDR frequencies and essentially the heating of the damaged regions. There is a vast amount of literature that covers frictional heating and contact temperatures [13-18], which can be used to determine the heat generated by damage due to nonlinear ultrasound effects. Material nonlinearity of damaged regions, in terms of nonlinear harmonic generation (due to ultrasound excitation) have been widely used over the past few years as a reliable signature for material flaws detection in metallic and composite structures [19-24]. Material nonlinear effects are defined by two basic forces: slipping/sliding of an interface and clapping (opening and closing of an interface/crack/delamination). Thus the heating mechanism can be assumed to result from a mixture of frictional heating due to the rubbing (in-plane forces) of the rough surfaces of the delamination zone as well as clapping (out-of-plane) of delamination regions. Contact due to clapping can be assumed to follow Hertzian contact theory between two elastic bodies with curved surfaces. This theory determines the vertical displacement of surface contact points (i.e. delamination layers) from which the normal stress can be determined [25]. Thus heat is generated due to the compressive force generated by this mechanism and can be assumed to results in elastic material behaviour. The mechanics for the movement of delaminated regions caused by the small stress exerted by ultrasound waves can be assumed to result

in: frictional rubbing of contact regions of damage interfaces and viscoelastic losses (due to hysteresis) during the loading and unloading cycles of ultrasound excitation. In-plane displacements are very difficult to measure, for this reason the out-of-plane displacement was measured using a Laser Vibrometer (LV). In terms of frictional heating this can easily be described as the transformation of mechanical energy into internal energy or heat. For the purposes of this piece of work it can be assumed that all frictional energy is dissipated as heat which is conducted into the contacting bodies at the actual contact interface [26]. Tribologists mainly focused on the behaviour and failure of sliding components, where surface and near-surface temperatures can change the structural properties of the sliding materials (resulting in wear). It can be assumed that due to the material properties of composites (high melting points) heating caused by friction from ultrasound excitation can be assumed to be purely elastic in behaviour and does not result in any irreversible state changes such as melting, softening or damage to the material. The conversion of mechanical energy into heat can be evaluated using the theory of thermoelasticity. A number of techniques such as lock-in IR imaging have been proposed which rely on this principle [27-30]. In sonic lock-in thermography, typically a low frequency (10-50 mHz) sinusoidal amplitude modulation of the acoustic excitation source is coupled with lock-in (i.e. at the same frequency as modulated signal) IR imaging. As the result of lock-in averaging at the modulation frequency, an amplitude and phase images are obtained after several minutes of excitation/imaging and data processing. Subsequently, defects may be discerned as local amplitude and/or phase changes associated with periodic thermoelastic temperature variations, which for example can appear as phase lags in the vicinity of the damage/defect compared to the phase patterns elsewhere on the structure.

Composite materials present a two-fold problem [31]: (i) the stress field associated with a typical fibre/matrix composite is essentially discontinuous thus quantitative studies on the microscopic scale are not practical, and (ii) in general composite structures are orthotropic therefore there can be markedly different mechanical properties in the three principle directions thus simple theories devised for isotropic mediums are not sufficient. In order to compare experimental results with computational models a nonlinear coupled structural-thermal 3D finite element (FE) model was developed, in order to assess the dynamic mechanical and thermal response of the structure driven by harmonic loading. Initially an experimental nonlinear ultrasound method is used to determine the LDR to evaluate BVID in the stiffener panel. Given that the production of further harmonics can be related to damaged regions, the second harmonic (twice the excitation frequency) was measured over a range of frequencies for the given test piece in order to assess which frequencies gave rise to the largest second harmonic amplitudes. This indicated which excitation (fundamental) frequency gave the highest levels of clapping/rubbing of the damaged regions, and thus heating. These frequencies were then evaluated by measuring the relative temperature rise at the centre of the damaged regions.

1.2. Nonlinear Ultrasound Stimulated Thermography

Nonlinear Ultrasound Stimulated Thermography (NUST) falls under thermographic NDE techniques which have the potential to provide quick evaluation of damage in materials. The NUST method focuses on nonlinear narrow sweep excitation (NNSE) between frequency ranges which exhibit large nonlinear responses, multiples of the fundamental excitation frequencies (i.e. 2^{nd} and 3^{rd} order harmonics). The NNSE methodology is expected to increase the probability of exciting at LDR and heat generation in damaged areas [32]. Active traditional thermography (heating or cooling methods) suffer from inadequate sensitivity to small defects, due manufacturing processes and safety standard requirements these methods are becoming less effective. Another factor with these techniques is that these methods tend to be subjective and do not provide easy adaptation to an automated defect detection process. The excitation of the medium results in heat generation through the dissipation of mechanical energy at the crack interfaces by vibration. The outcome is the visibility of defects due to

the local generation of heat caused by friction and/or stress concentration and visualisation of the temperature rise around the defect is possible using a high-sensitivity infrared imaging camera. Traditional systems use an ultrasonic welding horn to excite components that results in large disadvantages in the process. The ability to control and reproduce the excitation is extremely difficult due to; the nonlinearity in the coupling between the horn and component, damage of the component can occur due to the large energy output of the horn and from decoupling between the tip of the horn and component (chattering). Current methods have moved to using PZTs as they provide many advantages, such as the excitation can be accurately repeated, controlled and altered, and they do not necessarily cause damage to the component (due to lower energy requirements). Techniques such as lock-in and transient thermography are only capable of detecting BVID close to the sample surface, up to 2mm, this limitation means that only thin composite components or situations where damage lies on the surface are applicable. Other methods such as vibration excitation shearography (or speckle pattern shearing interferometry) measure the out-of-plane displacement gradient of a sample's surface, relying on defects altering the material response to an applied stress (such as vibration excitation using a PZT). Disadvantages of these methods are the lengthy time taken to determine the excitation frequencies and plate modes can hide damaged regions. Active traditional thermography (heating or cooling methods) suffer from inadequate sensitivity to small defects, while manufacturing processes and safety standard requirements are resulting in these methods becoming less effective. Another factor with these techniques is that the methods tend to be subjective and do not provide easy adaptation to an automated defect detection process. Contrast-based methods that focus on subtracting reference pixels or pixel groups from time history of each pixel in the image in order to determine a contrast of the temperature time history of the area, require the identification of defect free areas to provide a reference point, which is not always possible. Other general limitations such as requiring low signal to noise ratios, large dynamic ranges (pulses of energy used to heat sample), high processing powers (computer), storage space and memory make these applications difficult for in field work and automation. Promising techniques such as pulse phase and thermographic signal reconstruction look to evaluate subsurface conditions by the examination of the time history of pixels independently, while traditional techniques focus on visual or numerical identification of changes in surface temperature contrasts, these methods have provided some benefits in terms of the measurement of size of defects and effects of noise on detection limits [33]. Thermographic techniques have been estimated to be up to 30 times quicker than underwater ultrasonic c-scan techniques, illustrating the ability to rapidly inspect large areas of composite materials [34]. Thermal NDT/E relies on the generation of thermal waves in the sample which allow transient thermal images of the sample to be captured [34], the theory of heat conductivity including differential equations on the propagation of thermal waves has been extensively discussed by Almond and Patel [35]. A novel NNSE method was qualitatively assessed which requires no prior knowledge of defect/damage locations. This method showed that the assessment process could be simplified while increasing the probability of detection.

1.3. Experimental Setup and Equipment

1.3.1. Test Sample and NUST Equipment

A waveform generator (TTi-TGA12104) was connected to an amplifier (Piezoshaker-Amplifier HVA-DB100, includes vacuum pump) and piezoelectric transducer (Piezoshaker PS-X-03-6/1000) in order to provide excitation ranging from 20kHz to 30kHz at 200V. A vacuum pump and sucker attachment was used to attach the transducer to the test samples. The infrared camera used was a mid-wavelength infrared device (CEDIP Jade 3 MWIR 3-5 μm) that uses an electrically cooled indium antimonide detector and has a frame rate of up to 150 Hz, a resolution of 320 x 256 pixels (vertical x horizontal) average NeDT of 30 mK. A single frequency sinusoidal continuous wave form was generated and used to excite the damage regions for the LDR tests while thermal images were recorded by the camera. A narrow sweep excitation between 20 kHz-30 kHz was used to evaluate the ability of the NNSE method.

The impacted sample was a composite stiffener panel featuring a width of 577 mm, length of 797 mm and thickness of 5.5 mm; the composite layup and material characteristics are provided in Section 1.4.5. The sample consists of three stiffeners running the length of the panel. The panel had four areas of BVID, 2 between stiffeners 1 & 2 and 2 between stiffeners 2 and 3. For the purpose of this paper damages A, B and C have been focused on. BVIDs were introduced by low velocity impact damage (8-10 Joules). Figure 1 below shows the modelled stiffener panel, while Figure 2 shows the damage locations (A, B and C), stiffener locations and the area evaluated using the LV.

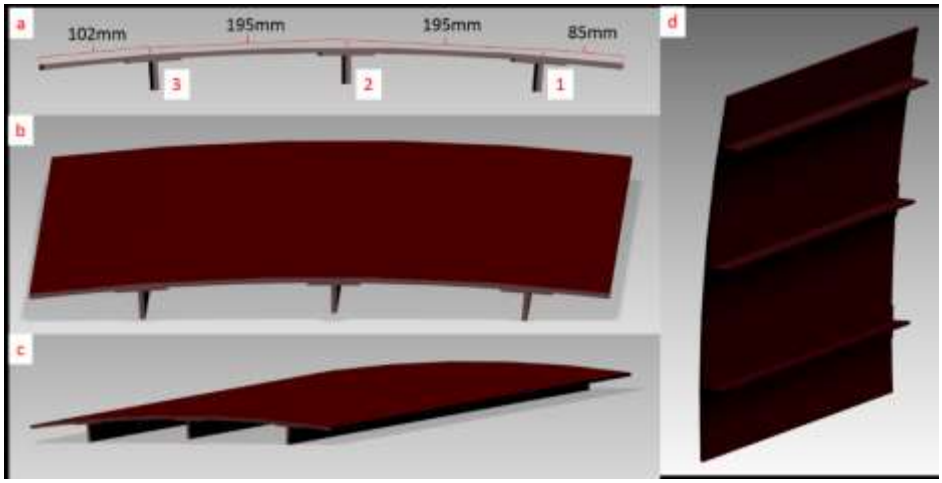

Figure 1: Stiffener Panel: (a) Side View -stiffener locations, (b) Side and Top View, (c) Oblique View and (d) Bottom View.

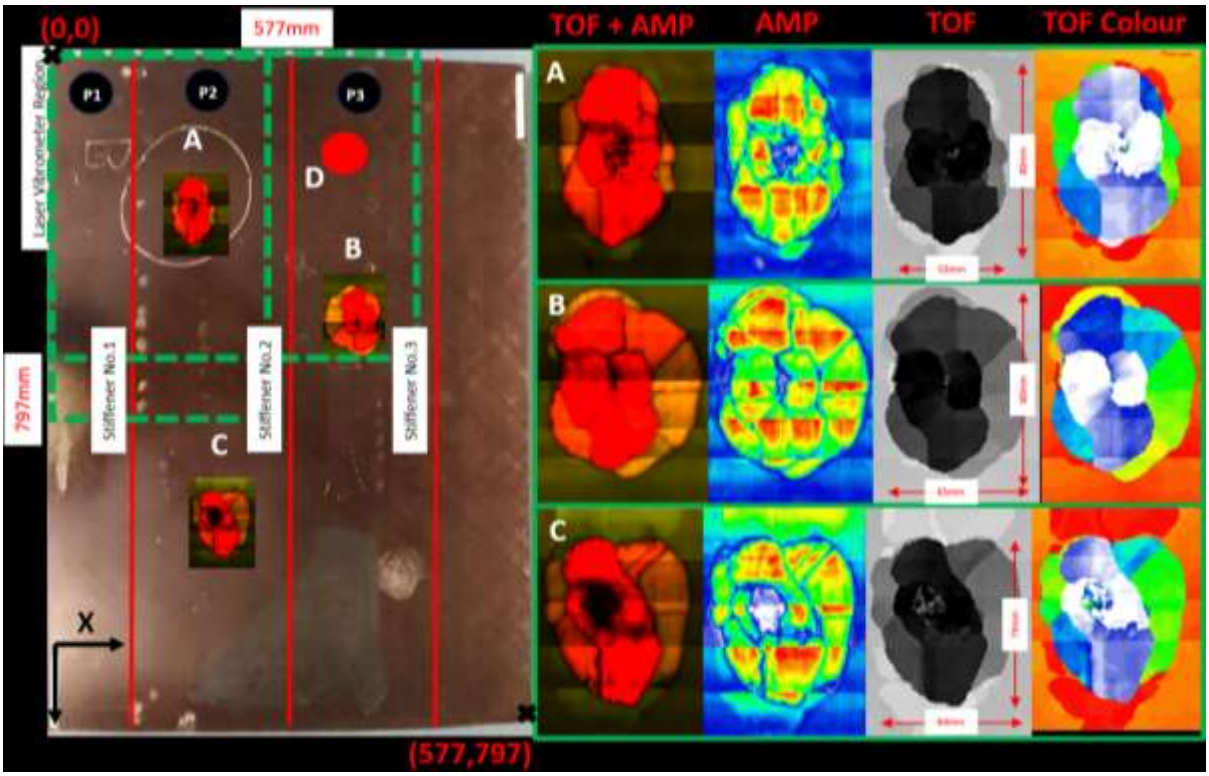

Figure 2: Composite stiffener panel characteristics, including: stiffener locations, damage locations and phased array assessment.

Figure 2 above also shows the damage evaluation results found by using a phased array system. The system comprised of a 128 element probe of which 64 elements were used to conduct a stepped linear C-Scan of the damage area using steps of 32 elements. Four methods were used to evaluate the damage regions: Time of Flight and Amplitude (TOF + AMP), AMP, TOF and colour TOF. It is clear to see that substantial delamination has occurred in these locations and that delamination becomes larger

through the thickness of the sample. Using these results it is possible to assess the size of the delaminated regions. Using the coordinate system shown in Figure 2, with the top left corner of the panel having coordinates (0(x), 0(y)) and the bottom right (577,797) the position of the damage regions are: A (180mm, 180mm), B (382mm, 310mm), C (195mm, 547mm) and D (367mm, 115mm). The positions of the piezo locations are: P1 (42.5mm, 40mm), P2 (127.5mm, 40mm) and P3 (322.5mm, 40mm).

1.3.2. Equipment and setup for LDR determination

Two piezoelectric transducers were used to determine the LDR, the excitation (transmitting) transducer (PZT-Panametrics NDT X1020 100kHz 515345) was located at TA, TB, TC and T1 (for damage A, B, C and the section between stiffener 1 and 2, respectively) while the signal was captured (PZT-Panametrics V101 0.5MHz 707718) at RA, RB, RC and R1 (for damage A, B, C and the section between stiffener 1 and 2, respectively), refer to Figure 3 below. The waveform generator was used to generate the output signal sweep from excitation locations (T1, TA, TB and TC), while the capturing sensor (R1, RA, RB and RC) was connected to an oscilloscope (Picoscope 4244) and PC. Transducers and sensors pairs were positioned 150mm apart and coupled to the surface using gel in an identical manner.

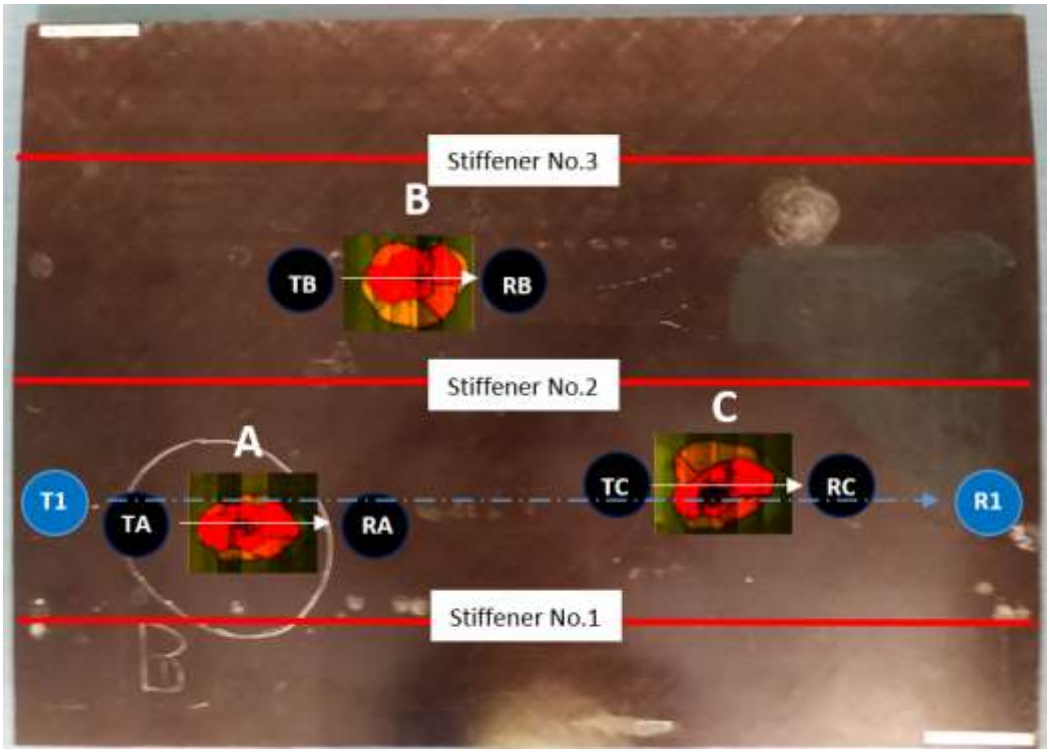

Figure 3: Location of Piezoelectric Transducers for LDR frequency evaluation.

A frequency sweep was conducted from 20 kHz to 30 kHz in order to determine the LDR, which was determined by using the fundamental frequency of the highest second harmonic response (between 40 kHz and 60 kHz). This was done for damage locations A, B and C. The LDR frequencies were then used when conducting the NUST tests. Further to this, a full length sweep between stiffeners 1 and 2 (light blue – T1-R1) was conducted in order to compare to the results of the individual LDR responses for damage A and C. The images captured using the infrared camera was processed using a background subtraction method. Figure 4 below shows the frequency response for the three damaged regions, with Table 1 outlining the fundamental frequencies of the largest second harmonic response. The raw output (directly from amplifier) is shown in green, while the results received from the stiffener panel are

shown in blue (material resonance). When reviewing the peak responses of the second harmonic it can be seen that these frequencies do not necessarily relate to the highest fundamental frequency response (material resonance), thus they can be considered to be LDR frequencies. The third harmonic responses have also been highlighted in the figure. The three highest responses common to all the damage regions were used as these were the most likely to generate the largest amount of heat.

It should be noted that the generation of harmonics can be directly related to the presence of damage within a material, thus these responses in the frequency domain can be related to vibration at the damage region with the highest response most likely relating to the LDR frequency. Nonlinear generation was investigated in order to determine whether it had the ability, not only to generate heat, but as an evaluation tool to determine which frequencies to excite.

Under traditional thermosonics techniques a very wide band frequency excitation method is generally used with a high powered welding horn (issues highlighted in introduction) while individual frequency excitation requires that a large amount of time is spent determining which frequency will excite the damage region (which can be considered a trial and error process). Furthermore, using a sweep methodology and determining excitation frequency from the highest fundamental responses does not always result in heating of the damage, due to the fact that these responses are likely to be resonance modes rather than the local defect resonance. The objective of selecting the excitation frequency from the nonlinear response is to ensure that the frequency chosen will in fact result in heating in the damage region, which is an improvement to the current methodology used.

In Figure 4 the vertical coloured bands refer to the selected excitation frequencies for the fundamental, second and third harmonics. For example in Figure 4 (a), the first brown line from the left refers to 21.420 kHz (the fundamental frequency), the second brown line refers to 42.840 kHz (2 x 21.420 kHz, the second harmonic) and the third brown line refers to 64.260 kHz (3 x 21.420 kHz, the third harmonic). The excitation frequency was determined using the highest response between 40 kHz and 60 kHz (the second harmonic region – highlighted by a blue box with a red border), the highest peaks were determined within this region and divided by two to determine the fundamental (excitation) frequency.

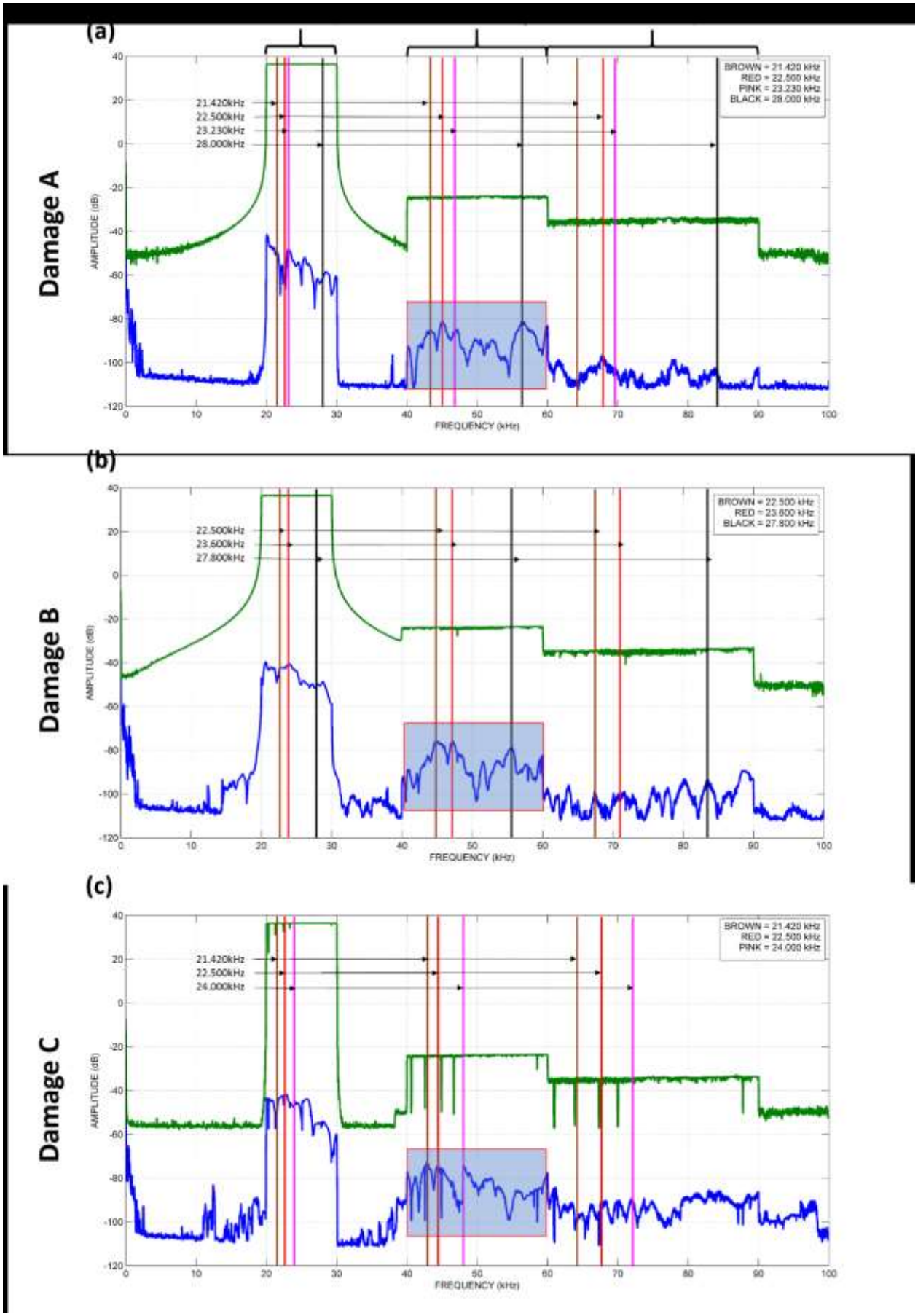

Figure 4: Frequency selection process according to amplitude of second harmonic for damage A, B and C.

Damage A (kHz)	Damage B (kHz)	Damage C (kHz)
21.420	22.500	21.420
22.500	23.600	22.500
23.230	27.800	24.000
28.000		

Table 1**:** Top frequencies according to highest second harmonic (nonlinear response).

One of the issues facing nonlinear ultrasound techniques is the generation of nonlinearities from equipment, these effects are presence especially when exciting with high power usually produced by amplifiers and waveform generators. The amplifier response has been included in Figure 4 (green) to show that there is in fact equipment based nonlinearities produced, it would unrealistic with current equipment capabilities to expect no equipment based nonlinearities. Another source of equipment based nonlinearities are generated by the contact between the transducer and the test specimen, which is a result of clapping or rubbing between the contact interfaces (transducer and surface of the sample). If equipment based nonlinearities were the overriding response, similar nonlinear effect should be seen from the transducer/sensor pairs (TA-RA, TB-RB, TC-RC). However, this is not the case here and the nonlinear response can be considered a material response. Furthermore, as two different transducers were used (one for LDR determination, the other during NUST), if coupling issues existed the frequencies determined by the LDR transducer/sensor pairs would not excite the damage locations during NUST experimentation.

Knowing that these responses are nonlinear responses, the focus is to determine which nonlinear response corresponds to an LDR frequency. LDR by definition is a local effect (i.e. the response is only located at the defect region) whereas nonlinearities are generated at damage regions and propagate from these regions, it is important to clarify that deconstructing these into two different entities is not the purpose of this work. LDR and nonlinear generation from damage regions are inherently coupled, i.e. if nonlinearities are produced due to nonlinear phenomena at a damage region and this occurs at an LDR frequency this response at this region will be amplified. Likewise if the fundamental frequency occurs at LDR this response will be amplified.

1.4. Numerical Finite Element Modelling

A numerical coupled structural-thermal model was developed in order to show the dependency of the (1) excitation position (P1, P2 and P3), (2) frequency of excitation, (3) distance between the piezo transducer and the damaged region and (4) location of excitation source relative to the stiffener positon. Considering the ever-increasing computing power and numerical efficiency of the computational methods, it is feasible to use commercially available FEA software tools to perform elastic wave propagation analyses on complex structures typical found in the aerospace industry, such as a CFRP composite stiffener panels. In this study, a commercial FEA solver LS-DYNA® was used for this purpose due to its world-class capabilities in simulating highly non-linear dynamic phenomena.

1.4.1. Finite Element Method

In order to model a dynamic mechanical and thermal response of the structure driven by the harmonic loading, a coupled structural-thermal 3D FEA was performed. In dynamic FEA, the solution (e.g. nodal forces and displacements) is obtained by satisfying equilibrium, which in the deformed body, can be described at each point by six independent equations (3 for translation and 3 for rotation). Principle of virtual displacement (PVD) is a single equation capable of enshrining these six equations. Considering a current domain Ω with a boundary Γ of a body, a weak form of the momentum equation can be stated using the PVD:

$$\int_{\Omega} \delta \mathrm{d}\, \boldsymbol{\sigma}\, d\Omega + \int_{\Omega} \delta \mathrm{v}\, \rho \dot{\mathbf{v}}\, d\Omega - \int_{\Omega} \delta \mathrm{v}\, \mathbf{b}\, d\Omega - \int_{\Gamma} \delta \mathrm{v}\, \mathbf{t}_{\mathrm{x}}\, d\Gamma = 0 \tag{2}$$

Where: $\delta \mathrm{d}$ is a virtual displacement, $\delta \mathrm{v}$ is a virtual velocity, $\boldsymbol{\sigma}$ is a stress tensor, ρ is density**,** $\mathbf{b}$ is vector of body forces and $\mathbf{t}_{\mathrm{x}}$ represents surface tractions (subscript x is used to avoid confusion with time variable). First term signifies the contribution of internal forces, whereas the second, third and fourth terms stand for contributions of inertial forces, body forces and surface tractions respectively. Eq. (2) is a governing equation and is discretised in space and time. Different numerical integration schemes were used for time discretisation of the structural and thermal models.

1.4.2. Structural Model

The governing equation [Eq. (3)] can be re-written as follows:

$$\mathbf{M}\ddot{\mathbf{u}} = \mathbf{F}^{\mathrm{ext}} - \mathbf{F}^{\mathrm{int}} \tag{3}$$

where: $\ddot{\mathbf{u}}$ is a second time derivative of the global displacement vector, $\mathbf{F}^{\mathrm{int}}$ is the global internal forces vector obtained by scattering each element vector into the global element array:

$$\mathbf{F}^{\mathrm{int}} = \sum_{e=1}^{n_{el}} \mathbf{L}_e^T \left[\int_{\Omega_e} \mathbf{B}^T \boldsymbol{\sigma} d\Omega \right] \tag{4}$$

where: Ω_e and Γ_e are the domain and boundary of each element respectively, n_{el} is the total number elements, $\mathbf{L_e}$ is the Boolean connectivity matrix, $\mathbf{B}$ is the matrix of spatial derivatives of shape functions.

$\mathbf{F}^{\mathrm{ext}}$ is the global external forces vector given by:

$$\mathbf{F}^{ext} = \sum_{e=1}^{n_{el}} \mathbf{L}_e^T \left[\int_{\Omega_e} \mathbf{N}^T \rho \mathbf{b} d\Omega + \int_{\Omega_e} \mathbf{N}^T \mathbf{t}_x d\Gamma \right] \tag{5}$$

where: $\mathbf{N}$ is the matrix of shape functions.

The lumped mass matrix is assembled as follows:

$$\mathbf{M} = \sum_{e=1}^{n_{el}} \mathbf{L}_e^T \left[\int_{\Omega_e} \rho \mathbf{N}^T \mathbf{N} d\Omega \right] \mathbf{L}_e \tag{6}$$

Equations (4-7) represent a system of nonlinear second order differential equations which are solved using explicit finite element code using direct time integration technique. Explicit time integration was used for structural response of the stiffener panel as this method is very well suited for physical problems which are on the order of milliseconds in duration. The global displacements at time $t + \Delta t$ using the central difference method is given by:

$$\mathbf{u}_{\mathrm{t}+\Delta \mathrm{t}} = \Delta \mathrm{t}^2 \mathbf{M}^{-1} \left(\mathbf{F}_{\mathrm{t}}^{\mathrm{ext}} - \mathbf{F}_{\mathrm{t}}^{\mathrm{int}} \right) - \mathbf{u}_{\mathrm{t}-\Delta \mathrm{t}} + 2\mathbf{u}_{\mathrm{t}} \tag{7}$$

where Δt is time increment or time step. Explicit time integration is computationally inexpensive for small durations and is conditionally stable - Courant stability criterion must be satisfied:

$$\Delta t < \Delta t_{critical}$$

$$\Delta t_{critical} \leq \frac{2}{\omega_{max}} \quad \textbf{(8)}$$

where ω_{max} is the highest natural frequency of the system, which for the assembled finite element model is bounded by the maximum frequency of the unassembled and unsupported elements. Physically this means that Δt must be small enough that the information does not propagate across more than 1 element per time step. Therefore, a choice of element size for finite element mesh is highly important. Material parameters and the size of finite elements directly affect the critical time step size. In present analysis, the maximum frequency of interest was of the order of 50 kHz which leads to a sampling rate of 1 MHz in case 20 points per wave length are desired. This information combined with the elastic properties of CFRP material yields an element size of 2.5 mm for an 8-node solid element. To achieve further increase in spectral resolution, an element size of 1.5 mm was used for the simulations.

1.4.3. Constitutive Model

In order to simulate a nonlinear elastic wave propagation in composite structures with distributed damage such as cracks and delamination, a nonlinear elastic orthotropic material model was implemented adopting the methodology devised by Ciampa et al [24, 36]. The model is based on the classical nonlinear (anharmonic) theory; in 1D, the nonlinear elastic modulus K can be expressed through a power series expansion of the stress with respect to the strain ε:

$$K = K_0\left(1 + \beta\varepsilon + \delta\varepsilon^2 + \cdots\right) \quad \textbf{(9)}$$

Where: K_0 is the linear elastic modulus, β and δ are classical second and third order coefficients of nonlinearity which can be determined experimentally. Since Equation (9) is a scalar model, it cannot be readily applied to investigate the response of orthotropic materials in 3D continuum such as the composite panel used in the experiments. By following the mathematical procedure outlined by Ciampa et al [36], this limitation can be overcome to arrive at the total elastic modulus due to nonlinear elastic material behaviour in 3D Cartesian space:

$$\widetilde{K}_i = \Lambda_i\left(1 + \beta\widetilde{\varepsilon}_i + \delta\widetilde{\varepsilon}_i^2 + \cdots\right) \quad \textbf{(10)}$$

Where: $\widetilde{K}_i$ is the total elastic modulus (i = 1,…,6) and Λ_i are the *Kelvin moduli*. This 6 x 6 nonlinear stiffness matrix is then transformed from Kelvin to Voigt notation (i.e. from $\widetilde{K}_i$ to **K**) for the implementation in the FE code [see Equation 5 and 8]. Hence, the Cauchy stress tensor $\boldsymbol{\sigma}$ can be written as:

$$\boldsymbol{\sigma} = \mathbf{K}\boldsymbol{\varepsilon} \quad \textbf{(11)}$$

Where: **K** is the total nonlinear stiffness matrix in Voigt notation and is updated at every time step in the numerical procedure and $\boldsymbol{\varepsilon}$ is the column array of material strains.

The constitutive model present in this study accounted for mechanical as well as thermal strains driven by the elastic deformation. The total strains are integrated in time and the principle strain components include local thermal strains due to thermal expansion of the finite elements:

$$\varepsilon_{k+1}^{m} = \varepsilon_{k}^{m} + \alpha^{T,m}\Delta T_{k} \quad (12)$$

Where: ε_{k}^{m} denotes the total element strain components in principle material directions at the time step k (i.e. the current state) with m = 1, 2, 3, $\alpha^{T,m}$ are the coefficients of linear thermal expansion and ΔT_{k} is a temperature increment at a current simulation step k. The temperature change is calculated based on the thermoelastic theory (Equation 2) for homogeneous orthotropic elastic body under adiabatic conditions [31]:

$$\Delta T_{k} = \frac{T_{k}}{\rho C_{p}} \sum_{m=1}^{m=3} \alpha^{T,m}\Delta\sigma_{k}^{m} \quad (13)$$

Where: C_p is specific heat, $\Delta\sigma_{k}^{m}$ is the stress increment in the principle material direction, T_{k} is the absolute temperature at the current time step and other terms have their usual meaning; note that at the initial time step T_{k} is a prescribed variable and was set to 20 °C in this analysis. The total temperature is then updated according to:

$$T_{k+1} = T_{k} + \Delta T_{k} \quad (14)$$

Subsequently, T_{k+1} is used as an input to the thermal solver (i.e $T_{k+1} = T_{n}$) which outputs the new value of temperature T_{n+1} for each finite element based on heat conduction which is then used as a current temperature $T_{n+1} = T_{k}$ during next structural time step.

1.4.4. Thermal Model

In the coupled solver configuration, a structural step is solved first with a subsequent thermal step for which a fully implicit backward difference method was employed; this is a recursive process until the specified termination time is reached. In the devised model, the harmonic excitation of the structure resulted in the generation of internal strains and stresses which in turn produced the associated temperature gradients. Therefore, the purpose of the thermal step was to compute the transient heat transfer caused by the simulated thermos-elastic effect. In 3D continuum, the generalised heat conduction equation is [37]:

$$\rho C_{p}\frac{\partial T}{\partial t} = \nabla\cdot\mathbf{q} + Q \quad (15)$$

Where: T is the temperature field, Q is the internal heat generation per unit volume and $\mathbf{q}$ is the heat flux vector defined by:

$$\mathbf{q} = -\mathbf{k}\cdot\nabla T \text{ or } q_{i} = -k_{ij}\frac{\partial T}{\partial x_{j}} \quad (16)$$

Where: **k** is the thermal conductivity tensor of order two; Equation (17) is the well-known Fourier's heat conduction law. Eq. (17) can be discretised numerically using the finite element method as follows [37]:

$$T_{n+1} = \left(\frac{\mathbf{C}_n}{\Delta t} + \mathbf{H}_n \right)^{-1} \left[\mathbf{F}_n + T_n \frac{\mathbf{C}_n}{\Delta t} \right] \quad (17)$$

Where: $\boldsymbol{C}$, $\boldsymbol{H}$ and $\boldsymbol{F}$ are the global heat capacity matrix, conductivity matrix and thermal force vector respectively and are equal to a summation of their respective element matrices over the total number of elements in the finite element domain and n denotes the numerical simulation step with $n = 1, 2, 3, \ldots$. A fully implicit simulation scheme was used to solve Equation (18). LS-DYNA performs time integration using a generalised trapezoidal method which is unconditionally stable [37]. With heat transfer taking place on a longer time scale than the mechanical deformation, the thermal time step can be allowed to be much larger than that of a mechanical time step - for this work, 50 times larger time step was used for the thermal analysis yielding adequate results.

1.4.5. Coupled Structural-Thermal Model for Wave Propagation

The constitutive model was implemented in LS-DYNA using the User Defined Material (UMAT) modelling interface. The geometry of the stiffener panel was meshed using fully integrated 8-node solid elements. The skin and the stiffeners of the CFRP panel consisted of 16 plies arranged in quasi-isotropic layup [0/90/-45/+45]2s, which were modelled ply by ply with 1 finite element through the thickness of each layer. Figure 5 shows the FE model of the stiffener panel with nonlinear material model applied to areas corresponding to the impact damage evaluated by C-scan during the physical experiment.

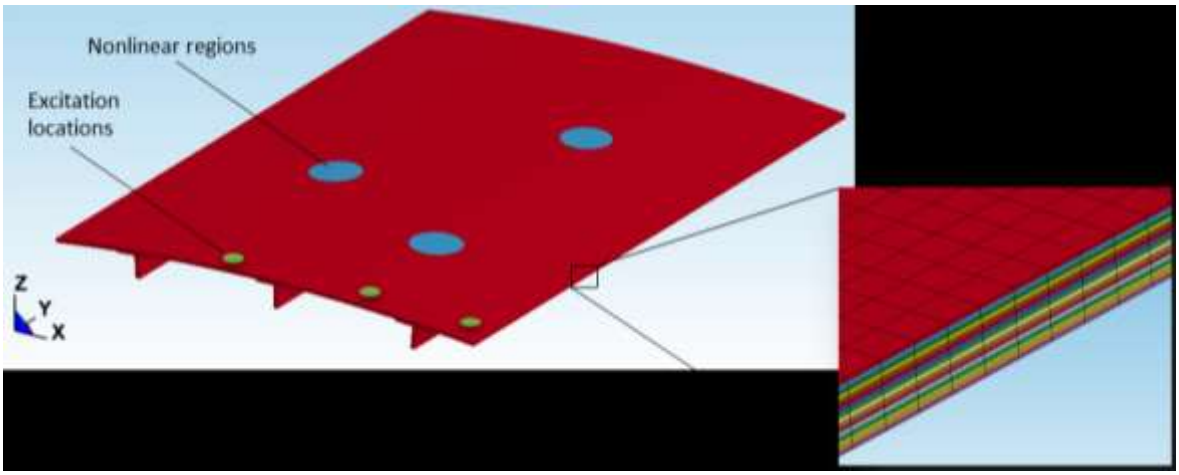

Figure 5: FE mesh.

The same material model was applied to all regions of the FE mesh with the only difference being the nonlinear parameter β which was set to be non-zero only for the non-linear areas of the model. With $\beta = 0$ the bulk of the mesh behaved as linear orthotropic elastic thermal material; $\beta > 0$ was specified for the damaged regions locally yielding a nonlinear response. Instead of attempting to determine this parameter experimentally, a sensitivity analysis was carried out in order to identify a suitable value. If β is too small, no significant nonlinearities may arise from the model, whereas large value of β can lead to numerical instabilities causing the simulation to fail. Although computationally expensive, the latter may be mitigated by scaling down the time step size using **CONTROL_TIMESTEP* [38] card

within LS-DYNA input deck. The values of β in the region of 1 x 10^{-2} to 1 x 10^{-4} worked sufficiently well in the current model with time step size pre-multiplied by the factor of 0.5 aiding the stability of the model. The level of nonlinear spectral response depends not only the values of the classical nonlinear parameters but also on the size of the nonlinear regions and the amplitude of the applied harmonic loading. A simple sinusoidal load was applied to the excitation nodes covering the area of the contact transducer used in the experimental setup:

$$s(t) = A\,sin(2\pi f t) \tag{18}$$

where A is the excitation amplitude, which was set to 50N, and f is the excitation frequency set to 22.5kHz. A burst of 3 ms was applied at the start of the simulation with wave propagation simulated for further 7 ms. The numerical problem was specified as a coupled structural-thermal analysis using the card **CONTROL_SOLUTION* with thermal solver settings provided in **CONTROL_THERMAL_SOLVER* and **CONTROL _THERMAL_TIMESTEP*. This way, mechanical strains and stresses were evaluated by the structural module, with adiabatic heat generation arising from the constitutive relationship, while the heat transfer within the FE domain was taken into account using the thermal solver. No heat transfer to the environment was considered.

ρ (g/cm^3)	E_1 (GPa)	E_2 (GPa)	E_3 (GPa)	G_{12} (GPa)	G_{23} (GPa)	G_{13} (GPa)	ν_{12}	ν_{23}	ν_{13}
1.56	121	8.6	8.6	4.7	3.1	4.7	0.27	0.4	0.27

$\alpha_{T,1}$* (C$^{\circ-1}$)	$\alpha_{T,2}$* (C$^{\circ-1}$)	$\alpha_{T,3}$* (C$^{\circ-1}$)	* Reference temperature of 20° C
-4.7e-7	3e-5	3e-5	

Table 2: Material properties used in the numerical model.

1.5. Stiffener Panel Wave Propagation

Figure 6, Figure 7 and Figure 8 show the wave propagation over time at 22.5 kHz for the three excitation positions (refer to Figure 2). The figures show the effect of the stiffener on the direction and symmetry (long parallel waves generated) of the wave. There is a clear reduction in the amplitude of the wave as it passes the stiffener (red line), this can be seen for piezo positions P1, P2 and P3. This reduction in amplitude has a direct effect on the ability of the wave to heat damaged regions, due to the reduction of stress in these regions. For piezo positions 1 and 3, the position of Damage A can be estimated by observing discontinuities in the wave front. Although after a short period of time it becomes difficult to evaluate the position of the damage as the structures modal shape becomes more apparent.

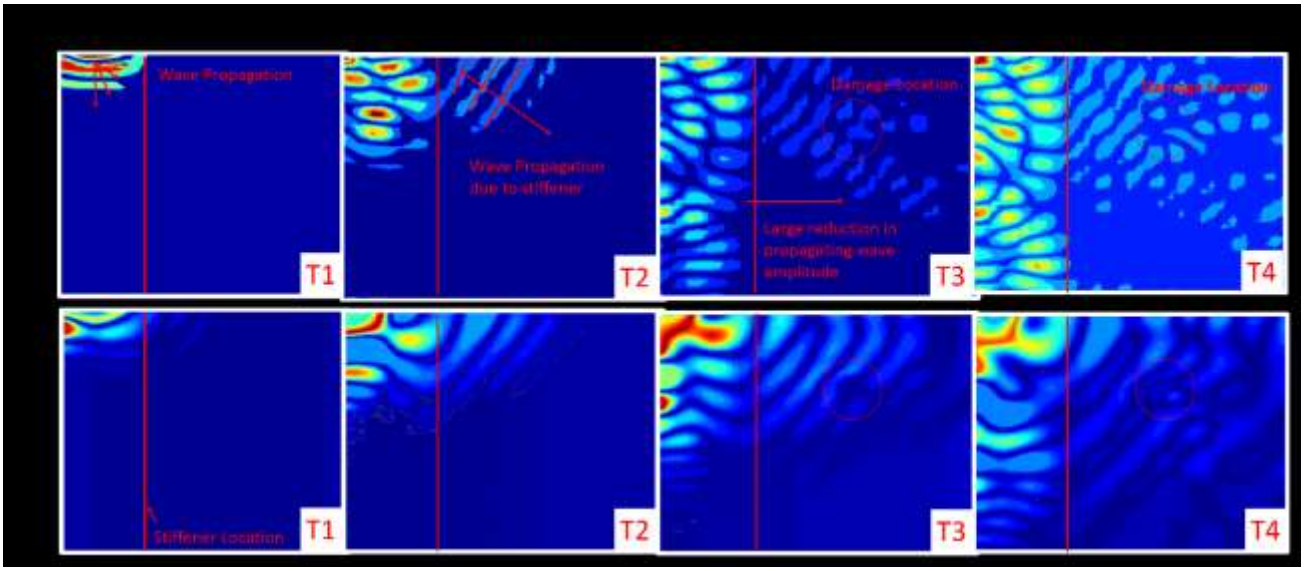

Figure 6: LV (a) and FEA (b) wave propagation from Position 1 for times T1 to T4 (22.5kHz Excitation, Out-of-Plane Displacement).

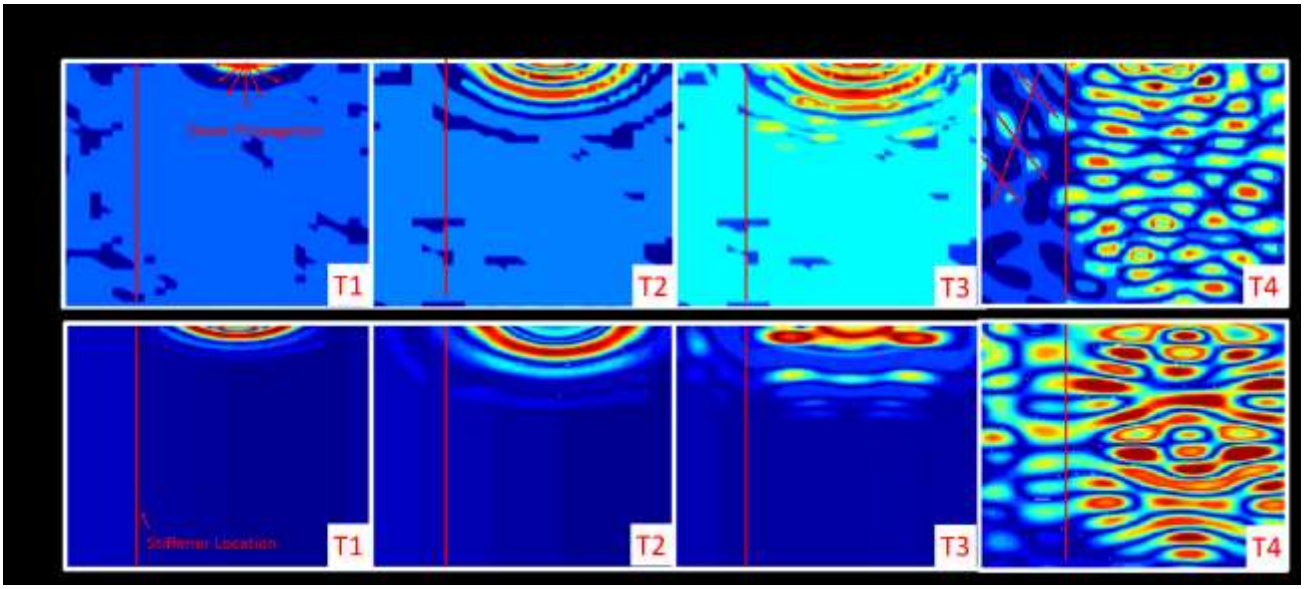

Figure 7: LV (a) and FEA (b) wave propagation from Position 2 for times T1 to T4 (22.5kHz Excitation, Out-of-Plane Displacement).

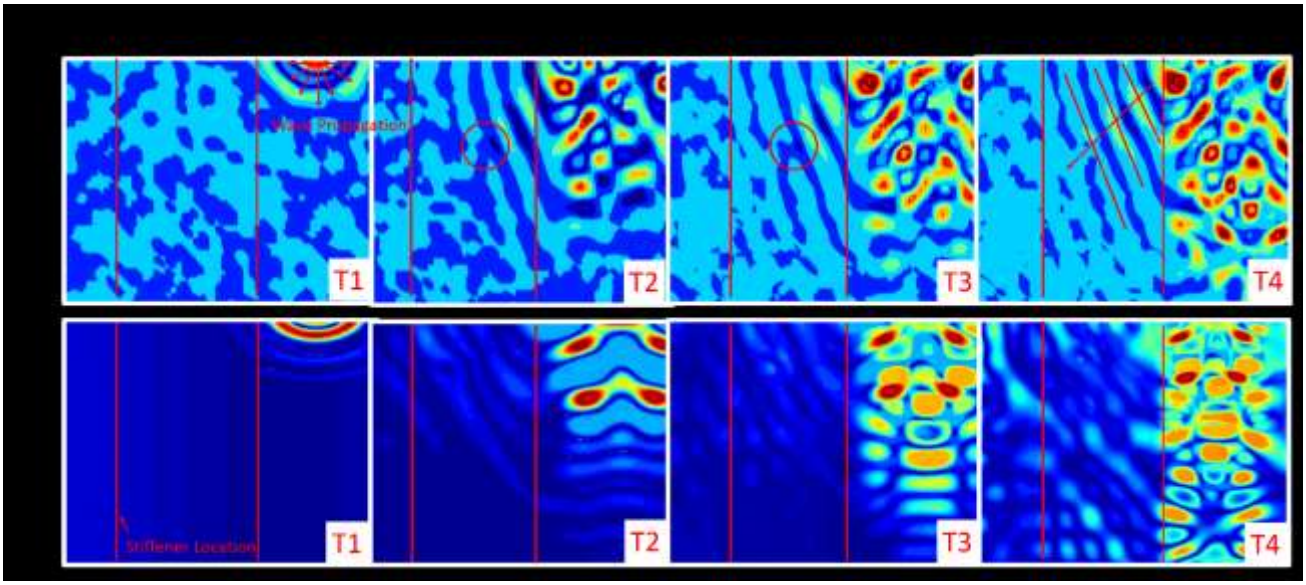

Figure 8: LV (a) and FEA (b) wave propagation from Position 3 for times T1 to T4 (22.5kHz Excitation, Out-of-Plane Displacement).

Figure 9 shows the results of modal analysis, which was performed using the implicit solver of LS-DYNA. Contours of out-of-plane displacement plotted for selected resonant frequencies in the range of 20 kHz to 30 kHz. This qualitatively confirms the importance of correct frequency selection. Considering the complexity of the stiffener panel and the frequency selected, it is possible to only excite individual sections between stiffeners. For example according to the modal analysis: 22508 Hz excites between stiffener 1 and 2; 22620 Hz excites between stiffeners 2 and 3, while 2466 Hz excites to the right of stiffener 3. This effect suggests that multiple frequencies should be considered in order to ensure that the NUST method sufficiently excites all regions of the panel. One of the big issues relating to sonic thermography techniques is the generation of sufficient energy to cause heating at defect and damage regions, by understanding the deformation of the structure at various frequencies it is possible to reduce the excitation energy required to sufficiently excite and generate heat in these regions.

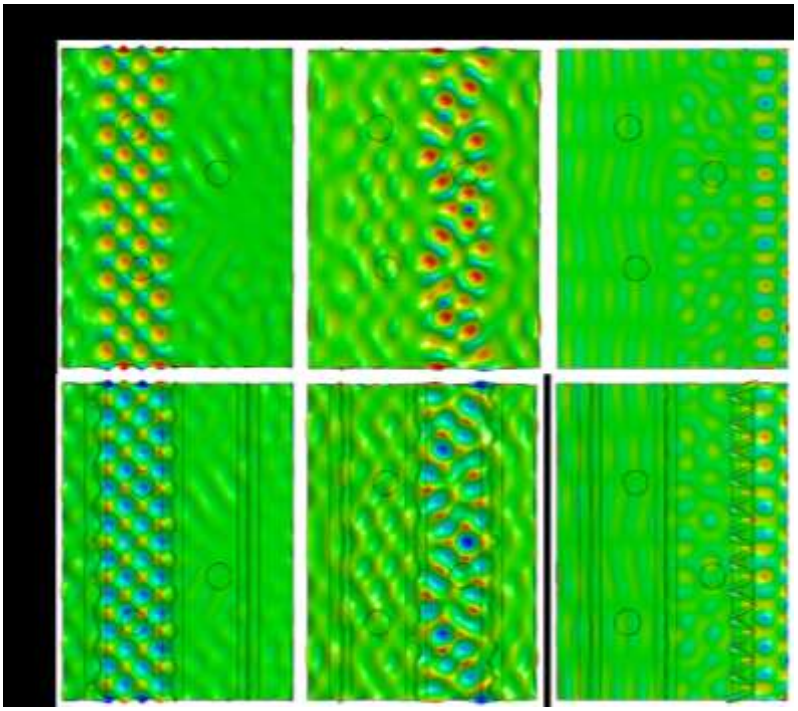

Figure 9: Modal FEA – contours of out-of-plane displacement.

1.6. Stiffener Panel Nonlinear Ultrasound Stimulated Thermography using LDR

Figure 10 below shows the general format for the NUST tests. The vertical red lines indicate the position of the stiffeners (1, 2 and 3 from the left), while the dashed green lines show the two areas evaluated using the LV. The ability of the NUST technique was evaluated using the LDR frequencies determined from the sweep analysis of the damaged regions (Figure 4).

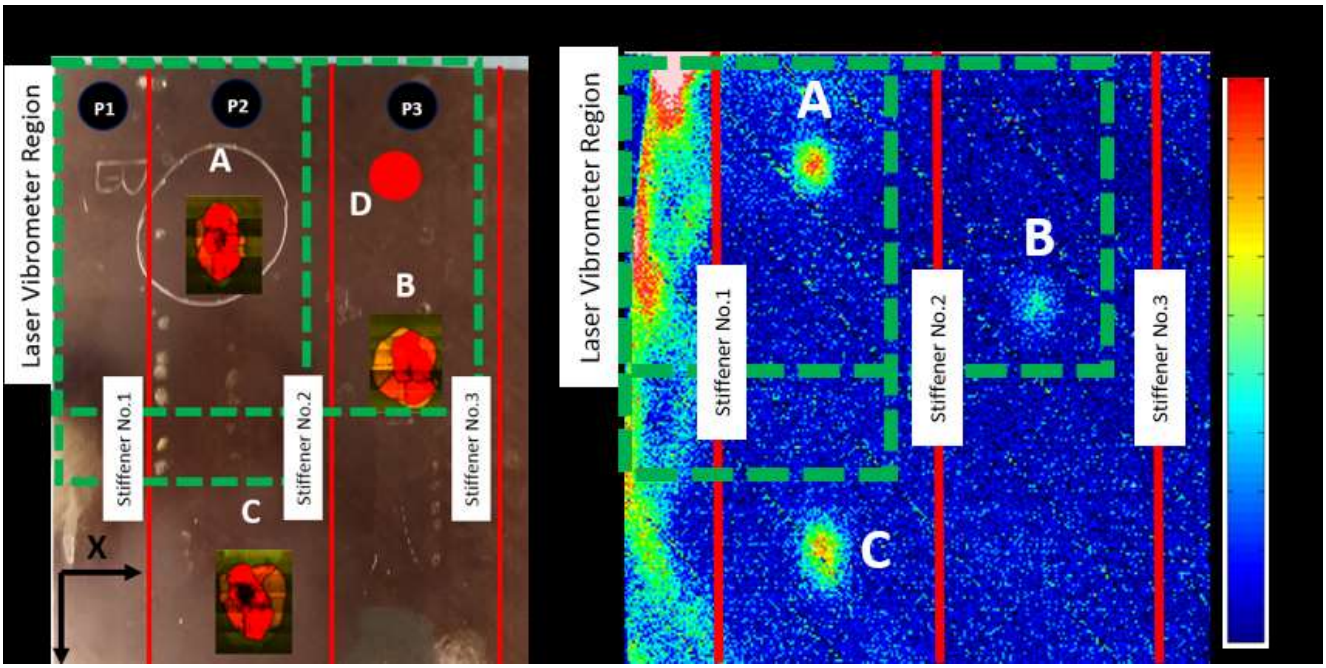

Figure 10: Stiffener and damage locations (a) and NUST (b) - Normalised Apparent Temperature Distribution using IR camera.

Figure 11, Figure 12 and Figure 13 show the results for frequencies 21.42 kHz, 22.5 kHz (common to all damage regions - please refer to Table **3**, for frequency information)and 23.23 kHz respectively.

The thermographic images of the BVID demonstrates that the heating is mainly produced in the core part of the delamination, this is confirmed by comparing the location of heating to the phased array results (Figure 2). Heating of damaged regions are amplified when excitation takes place on the same section of the stiffener panel, while heating is reduced when the excitation location and damage region is separated by a stiffener. This reduction of heating due to the stiffeners is clearly visible and confirmed by the wave propagation results from the previous section (Figure 6, Figure 7 and Figure 8).

Damage A (kHz)	Damage B (kHz)	Damage C (kHz)
21.420	22.500	21.420
22.500	23.600	22.500
23.230	27.800	24.000
28.000		

Table 3: Top frequencies according to highest second harmonic (nonlinear response).

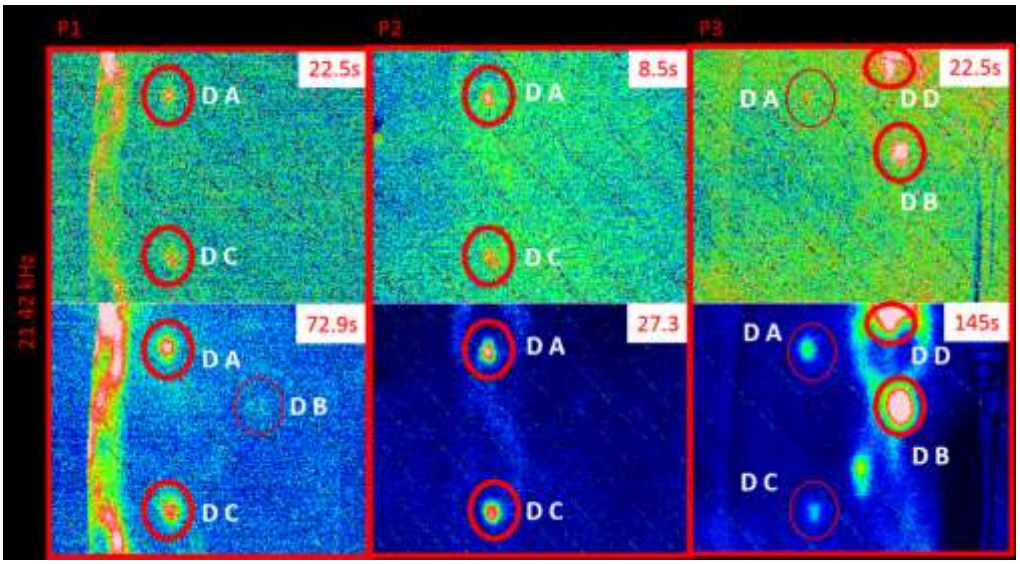

Figure 11: NUST results for the three piezo transducer locations (P1, P2 and P3) for various excitation times (21.42kHz Excitation) with damage regions labelled.

Figure 12 below shows the raw background subtracted images along with smoothed images of the thermal response during ultrasound excitation. It can be seen that damages B and D become clearer when the images are smoothed.

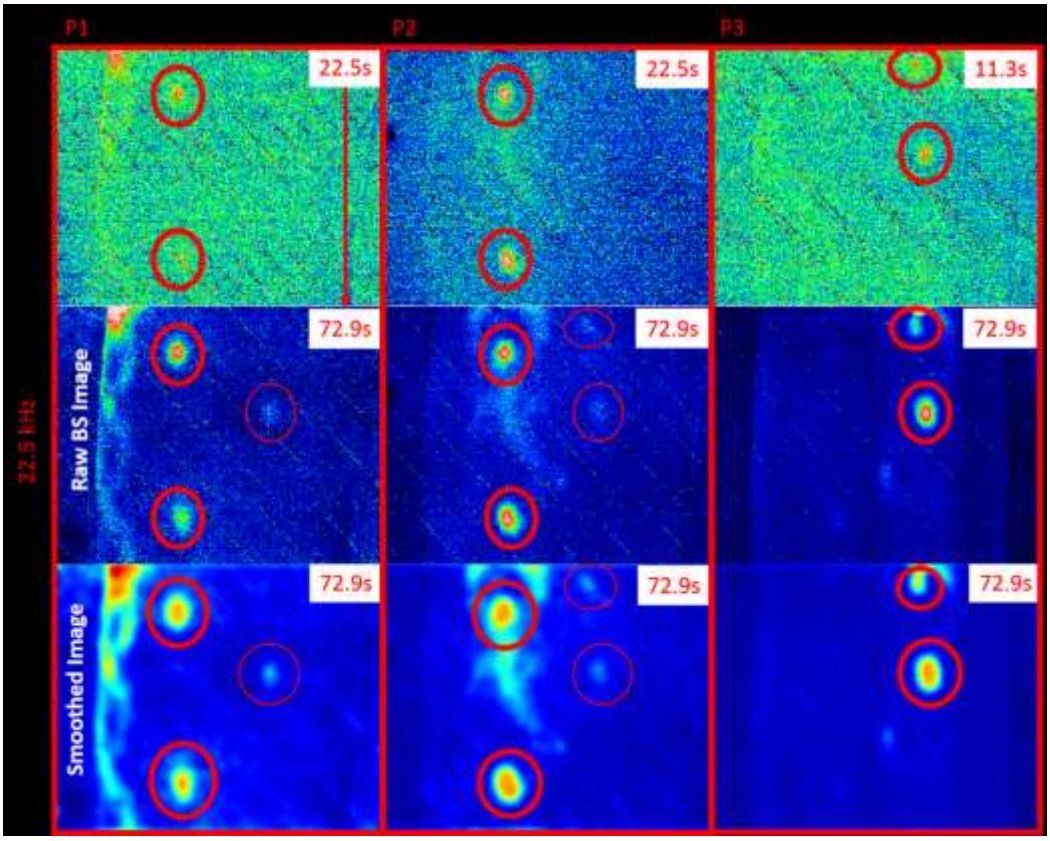

Figure 12: NUST results for the three piezo transducer locations (P1, P2 and P3) for various excitation times compared with smoothed images at 72.9s (22.5 kHz Excitation).

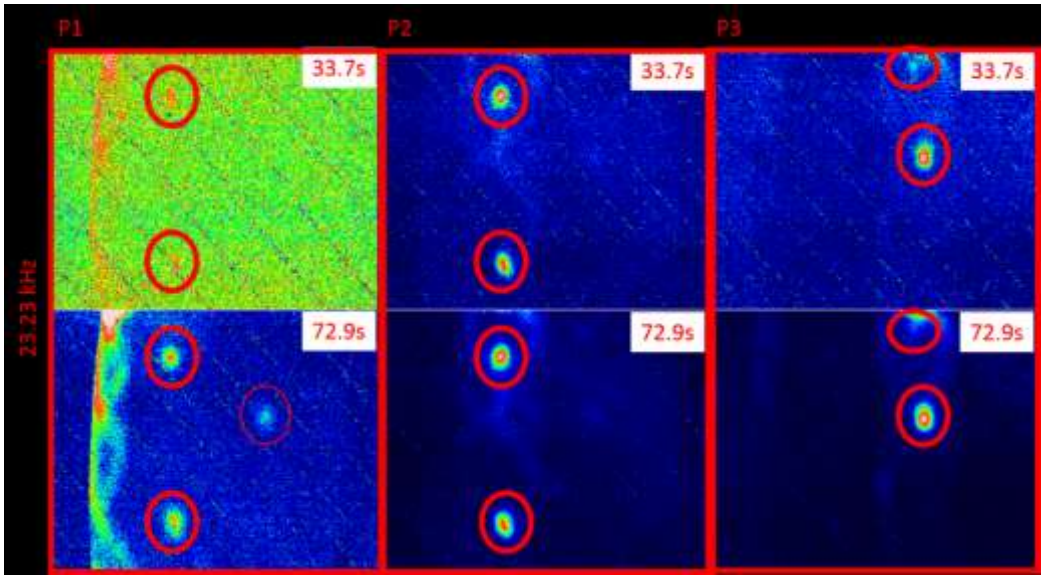

Figure 13: NUST results for the three piezo transducer locations (P1, P2 and P3) for various excitation times (23.23 kHz Excitation)

Heating of the BVID is clearly dependent on: (1) excitation position (P1, P2 and P3) as suggested by the modal analysis results (Section 1.5 – FEA and LV, Figure 6 to Figure 9), (2) frequency of excitation (Figure 11 to Figure 13), (3) the distance between the piezo transducer and the damaged region and (4) location of excitation source relative to the stiffener positon. These heating dependencies are not new findings and have been known for some time, but they make it difficult to evaluate samples using traditional methods due to the large number of unknowns.

1.7. Stiffener Panel Nonlinear Ultrasound Stimulated Thermography (NUST) using NNSE

Following the modal analysis results and NUST - LDR results from the previous section, it is clear that an alternative method should be used to improve detection capabilities of thermosonic methods. Issues such as wave concentration between stiffeners and the difficulty in determining LDR frequencies seriously impede the potential of such methods to be used for real world applications, mainly due to its lack of repeatability for defect/damage detection. The NNSE methodology, which focuses on exciting a narrow frequency band using a sinusoidal sweep, provides various advantages to standard single-tone burst methods to detect LDR [8]. In particular, large areas can be evaluated by understanding the general frequency response of the material (Figure 3, P1 to P2 blue) and the excitation is more likely to excite multiple LDR frequencies due to the sweep methodology. NNSE was conducted by exciting the structure between 20 kHz to 30 kHz with a sweep duration of 45 s, this was run for a total of 135 s (three sweeps).

Figure 14 below represents the relative temperature rise (blue line) versus the frequency response (red line, 20 kHz to 30 kHz). Figure 14 (a) and (b) plots the individual frequency response for damage A with its temperature rise, for the fundamental response between 20 kHz and 30 kHz (a) and for the second harmonic response between 40 kHz and 60 kHz (b). It can be seen that there is a clear correlation between the peaks of the second harmonic and heating, the fundamental response should not be ignored as it is expected that it results in a large contribution to the heating of damaged regions (which will be explored later).

Figure 14 (c) and (d) show the general material response between stiffener 1 and 2 from one end of the panel to the other. Although there are clear differences in the second harmonic responses between (b) and (d), there is still a good relationship between high harmonic responses and the generation (increase) in temperature at damage A. This relationship can be visualised in zones I, II, III and IV which have been highlighted in dotted boxes in Figure 14 (b) and (d) and Figure 15. Zones III and IV are a repeat of the frequency sweep in zones I and II and these peaks in the temperature profile correspond to specific frequency excitation in the stiffener.

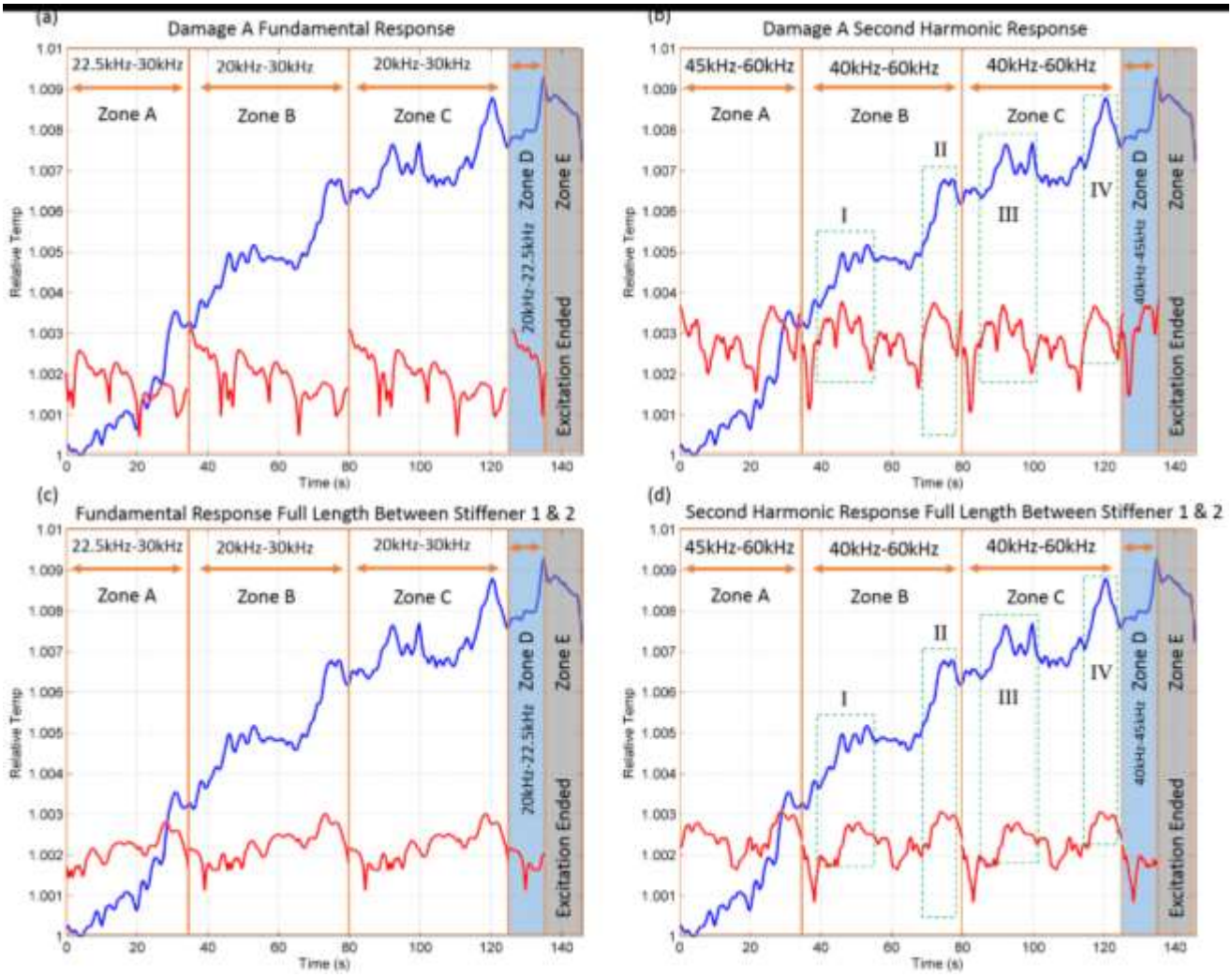

Figure 14: Relative temperature profile (blue line) during frequency sweep excitation compared with the fundamental and second harmonic response (red line) for damage region A (sweep range 20 kHz and 30 kHz).

Figure 15 below shows the superimposed image of the second harmonic frequency response vs. the temperature in the stiffener for zones I and II (Figure 14 (b)). It is clear to see that in image Figure 15 (a) the three frequency peaks (red) correspond to heating in the stiffener (three peaks blue). The delay in the occurrence of heating in the sample is due to delay in the propagation of heat, the same effect is also exhibited in Figure 15 (b). The incidence of these specific peaks found at the second harmonic also correspond to peaks found in zones III and IV (this relationship is also exhibited in Figure 14 (d)). The peaks shown in Figure 15 (a) and (b) are the four highest second harmonic response found for damage A, and as the figures show there is a direct relationship between the production of these harmonics and heat generated at damage A, thus an increase in heating has occurred as a result of these further frequency components being generated.

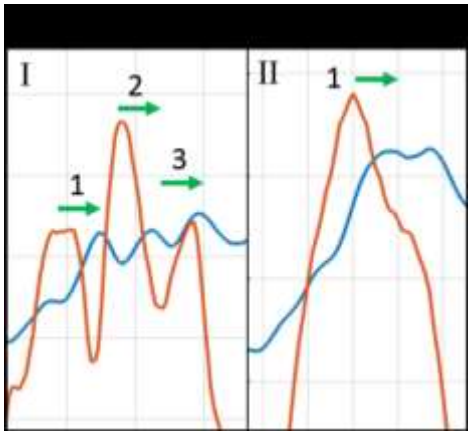

Figure 15: Relative temperature profile (blue line) during frequency sweep excitation compared with the fundamental and second harmonic response (red line) for region A damage response (sweep range I and II –**Figure 14** (b)).

Figure 16 shows the NUST results using the outlined NNSE method. It is clear to see that damages A, B and C are clearly visible using the IR camera while exciting from transducer position 1 (P1). These results show the ability and effectiveness of NNSE to excite multiple damage regions separated by multiple stiffener panels. Figure 12 (22.5 kHz, LDR) displayed similar results in that the three damage locations were visible when exciting from P1, although determination of the excitation frequency required prior knowledge of the damage location. Other LDR frequencies highlighted in the previous section were not effective in determining the damage locations using NUST when exciting from positions separated by stiffeners. These results agree with the modal analysis results, which showed that different frequencies excite different areas between stiffeners.

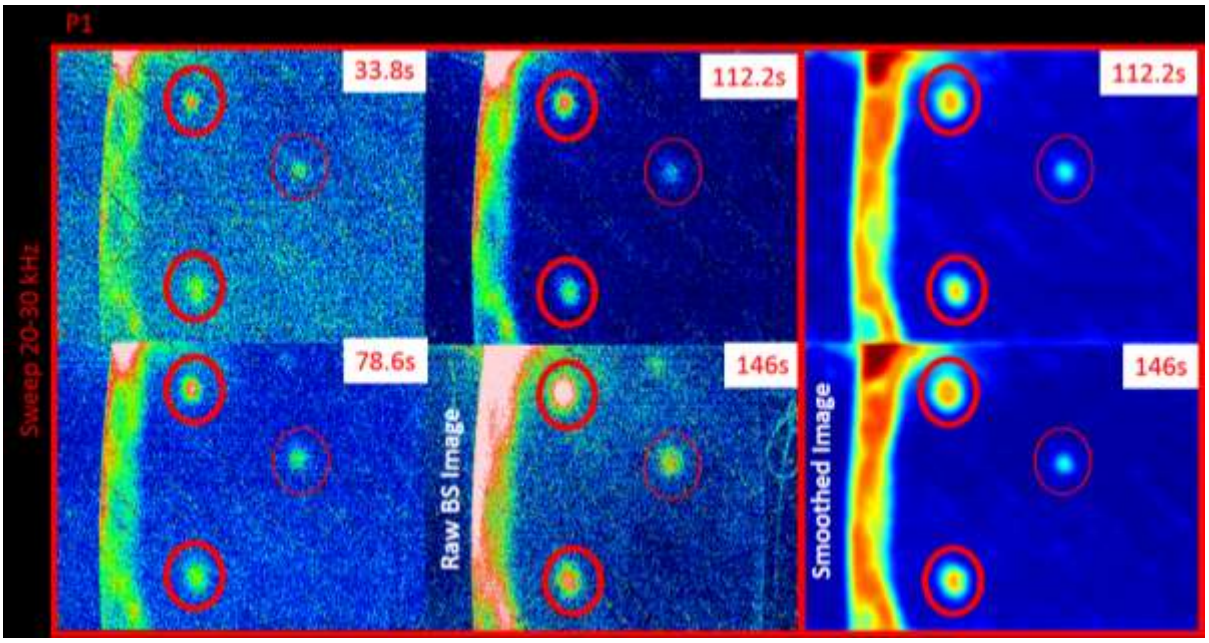

Figure 16: NUST results for transducer position (P1) while conducting a sweep between 20 kHz and 30 kHz.

1.8. Comparison between Nonlinear Ultrasound Stimulated Thermography, Laser Vibrometry and Numerical Model

The generation of the fundamental frequency and further harmonics (2nd and 3rd) were evaluated using a LV for the various testing positions P1 (Figure 18), P2 (Figure 19) and P3 (Figure 20). Refer to Figure 17 for transducer and damage locations and LV inspection region. Figure 18 and Figure 19

show that there is a clear generation of the fundamental, second and third harmonics at the damaged region clearly shown by the high amplitude response (FFT data) to the right of stiffener 1, exactly in the position of Damage A. This confirms that the frequency selection process has correctly determined harmonic responses that relate to LDR frequencies. Furthermore heating to the left of stiffener 1 follows a shape that is similar to that produced by the fundamental, second and third harmonic responses.

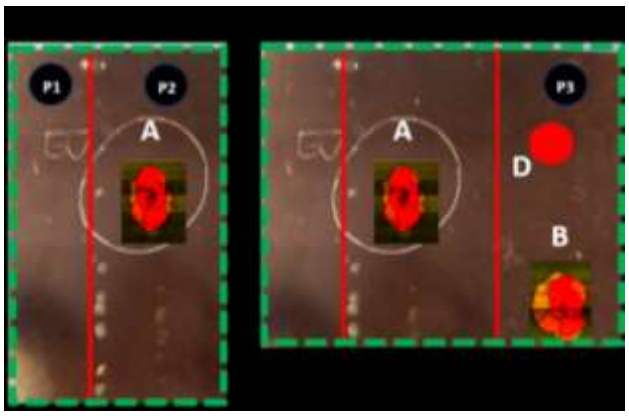

Figure 17: Excitation and damage locations for P1 and P2 (a-refer to Figure 18 and Figure 19) and P3 (b - Figure 20)

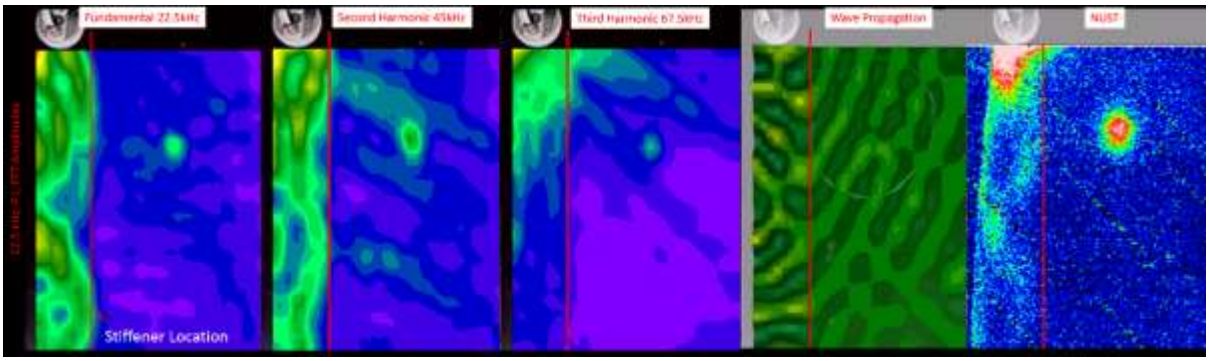

Figure 18: Laser Vibrometer Results compared with NUST (IR Camera, Temperature Distribution), transducer position 1 (22.5 kHz Excitation).

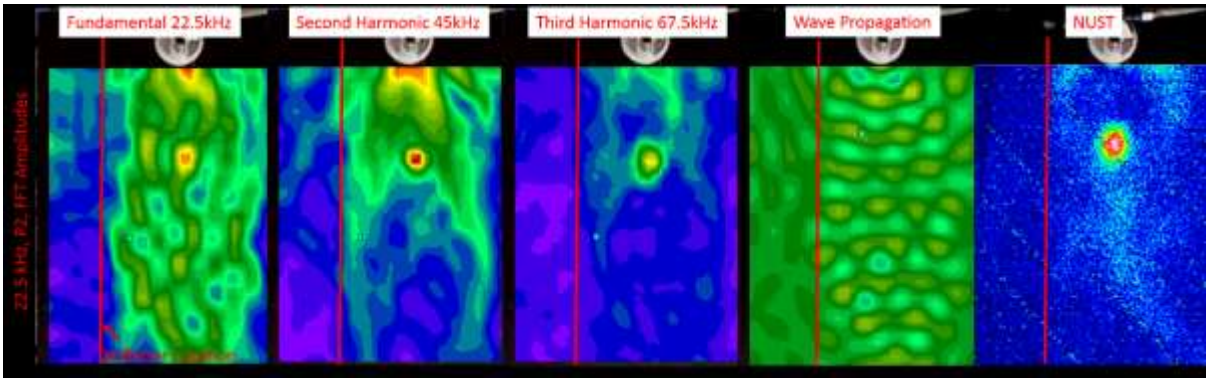

Figure 19: Laser Vibrometer Results compared with NUST, transducer position 2 (22.5kHz Excitation).

Unlike excitation positions P1 and P2; P3 does not exhibit large harmonic (2^{nd} and 3^{rd}) responses between stiffener 1 and 2 but does exhibit large harmonic responses to the right of stiffener 2. When comparing the NUST image to the production of harmonics (LV) only damage B and D can be clearly seen, this suggests that further harmonic excitation of the damage region provides significant heating and can be a significant factor in damage detection. The reduction of heating at damage A (P3) is a direct effect of the reduction in the propagating wave between stiffener 1 and 2 which is visualised in

the wave propagation image (Figure 20) and ultimately results in a reduction in the production of the 2nd and 3rd harmonics.

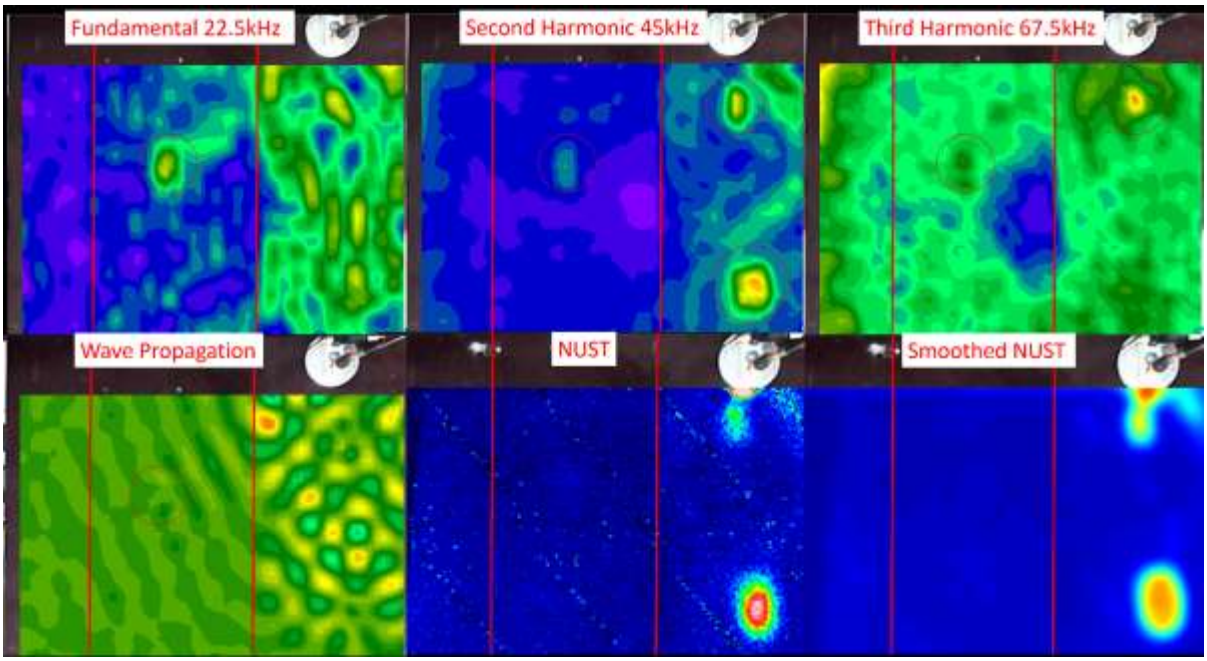

Figure 20: Laser Vibrometer Results compared with NUST, transducer position 3 (22.5 kHz Excitation).

Figure 21 shows a temperature distribution on the surface of the stiffener panel as calculated by the coupled structural-thermal FEA model. According to Equation 15, the heating was calculated based on the principle elastic stresses at finite elements. It is evident from the figure that there were localised regions of elevated temperature at the locations where nonlinear constitutive model was introduced (highlighted by dashed circles). When the constant of nonlinearity (i.e. β) was set to zero, no distinct temperature rise was produced at those locations. This signifies a link between the generation of the 2nd harmonic and the heat. Increasing the β parameter led to a nonlinear change in stiffness coefficients which subsequently led to the production of heat in the corresponding finite elements. The heating pattern was also dependent on the excitation location. However, no colour maps are present in this study as no attempt was made to quantitatively compare the results.

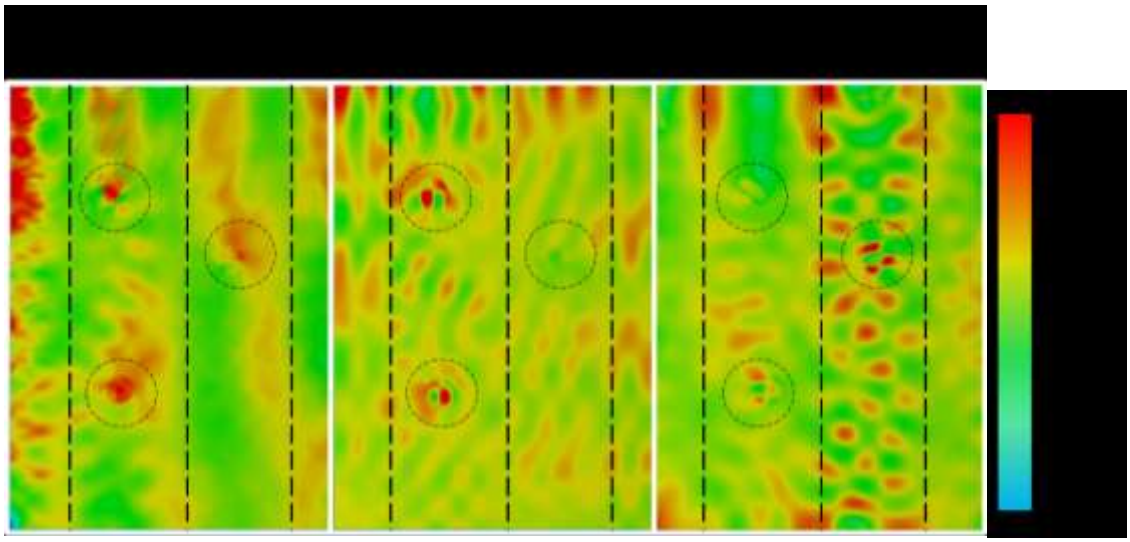

Figure 21: FEA thermal map (K) for various excitation positions.

Figure 22 (a) and (b) below, highlights the difference in the voltage (V) response between the fundamental and second harmonic for damage A and C. The amplitude of the fundamental is much larger than that produced by the second harmonic response, which is expected, but from the profile it is clear that the fundamental frequency generally results in a much higher excitation over the length of the panel. Whereas the second harmonic, exciting at LDR, only excites the damage regions. Comparing the LV results to the NUST temperature profile (Figure 22 (c)) it is clear to see that general heating (in areas other than the damage region) is driven by the fundamental frequency. This becomes clear as there is a thermal ridge that is evident in the fundamental LV results as well as the thermal temperature profile.

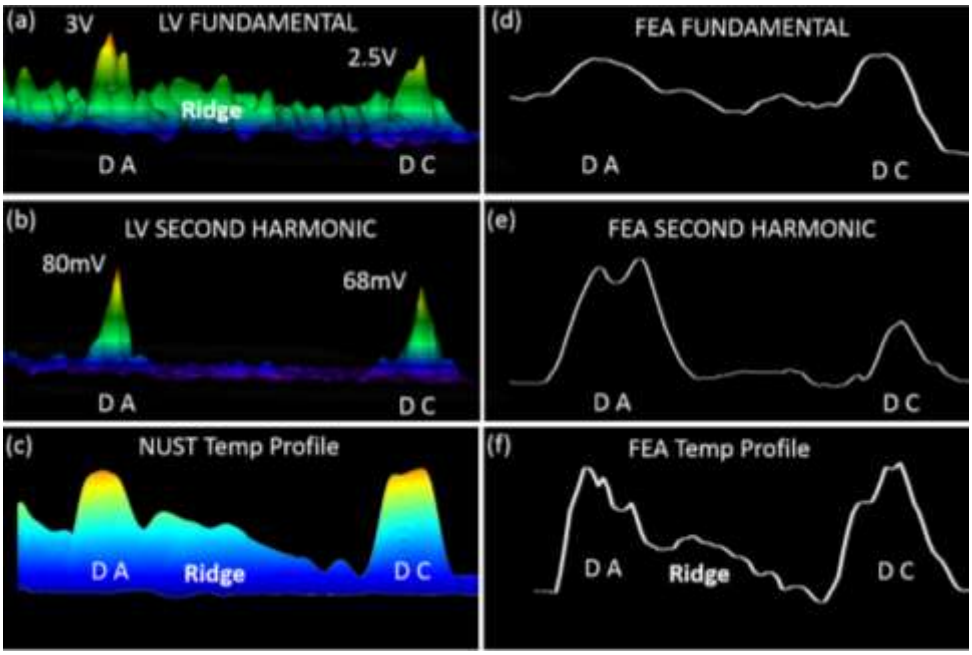

Figure 22: Fundamental Harmonic Amplitude (V, Voltage) for Damage A and C ((a) – LV, (d)-FEA), Second Harmonic Amplitude (V) for Damage A and C ((b) – LV, (e)-FEA), Thermal Profile from NUST ((c) – IR, (f)-FEA).

Figure 23 highlights the fact that this ridge is the result of the fundamental frequency response of the material, rather than heating due to the nonlinear material LDR frequency. Following on from the results shown in Figure 20, this confirms that the nonlinear frequency response at LDR causes significant heating that in that case was the critical factor in not detecting damage A (when exciting from transducer P3). Thus, as was hypothesised, due to the increase in heating at LDR (determined using the principles of nonlinear ultrasound) the required wave energy needed to cause heating is reduced.

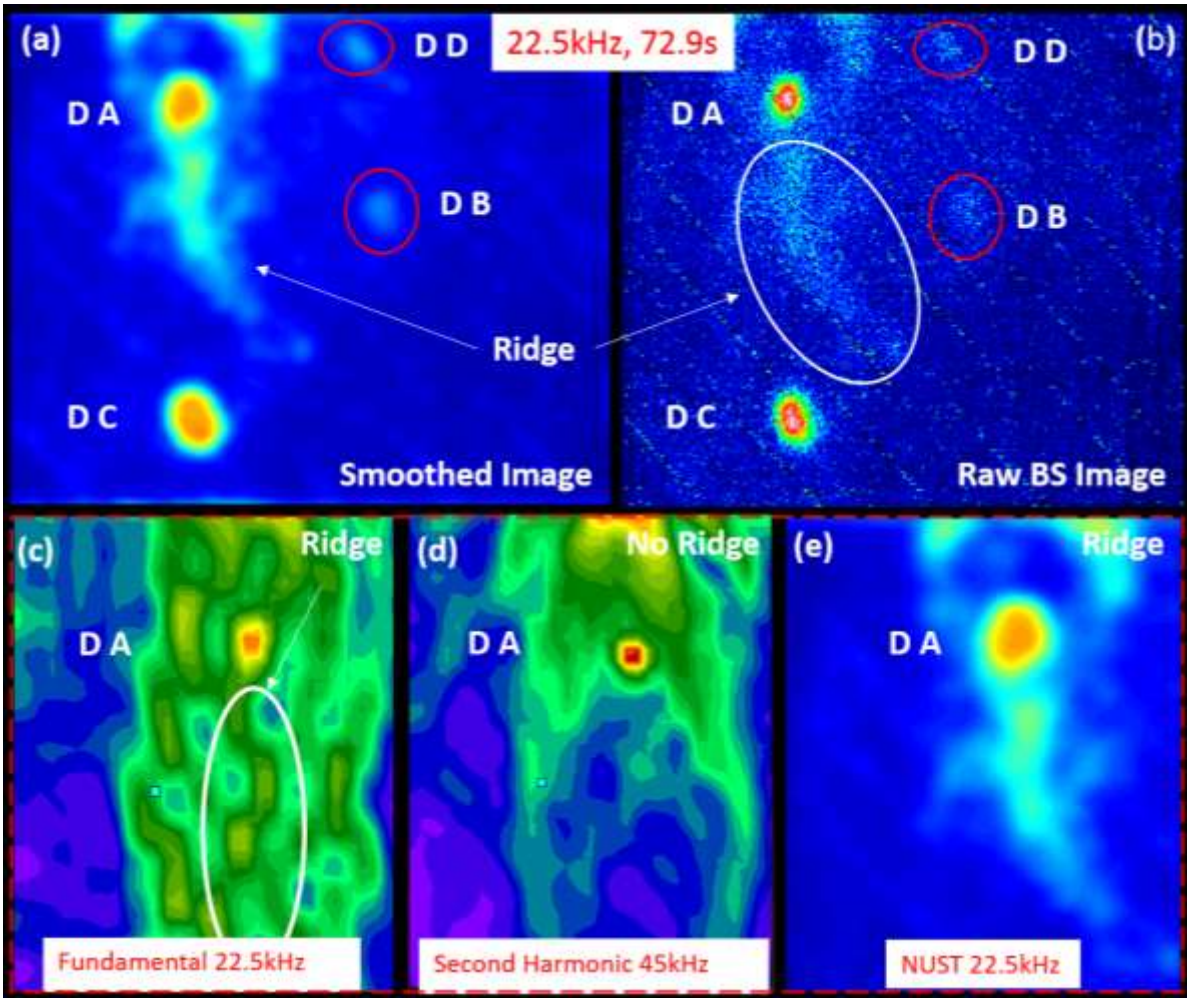

Figure 23: (a) Smoothed NUST Image, (b) Raw Background Subtracted NUST Image, (c) Fundamental Frequency Response Laser Vibrometer, (d) Second Harmonic Frequency Response Laser Vibrometer, (e) Smoothed NUST Image near Damage A (all for 22.5kHz excitation).

Figure 24 (a) and (b) below, highlights the difference in the velocity response between the fundamental and second harmonic for damage A. The amplitude of the fundamental is much larger than that produced by the second harmonic response, which again is expected and follows the voltage results from Figure 22.

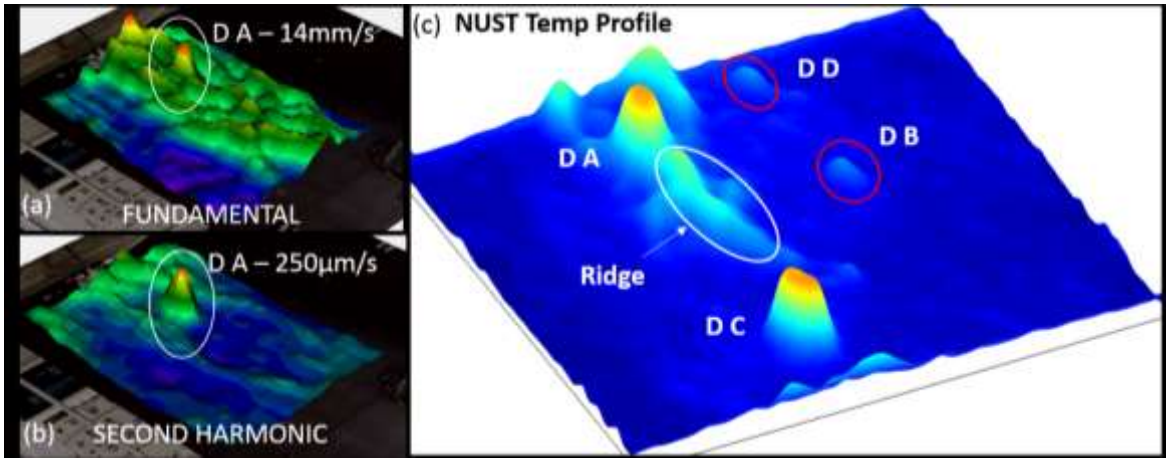

Figure 24: 3D representation of Damage A for the Fundamental (a) and Second Harmonic (b) in terms of velocity, (c) NUST smoothed temperature profile for the whole stiffener panel with damage A, B, C and D.

1.9. Conclusion

A novel Nonlinear Ultrasound Stimulated Thermography (NUST) technique is proposed for detecting and sizing barely visible impact damage in complex composite structures. This novel methodology relies on the nonlinear narrow sweep excitation (NSSE) to optimally identify the local resonance of a damaged region. NSSE focuses on exciting a narrow frequency bandwidth using a sinusoidal sweep and has various advantages to standard single-tone burst methods for the experimental estimation of the LDR frequency. Indeed, by understanding the frequency range that gives rise to the highest nonlinear harmonic response in the damaged material and exciting at the corresponding fundamental frequency range, NSSE increases the probability of single or multiple damage excitation and heating. Nonlinear ultrasounds were used to select the optimal input bandwidth of the sweep signals that actuated and intensified the LDR effect and, thus, the generation of frictional heat at damage location. This dramatically improved the efficiency and reliability of traditional thermosonics. To validate this concept, a complex composite stiffener panel was assessed with the NUST method and the experimental results were compared to those obtained with a laser vibrometer and an ad-hoc developed structural-thermal nonlinear finite element (FE) model. Whilst the laser vibrometer was used to understand the propagation of nonlinear waves generated at the damaged location, the coupled structural-thermal nonlinear FE model was employed to simulate the dynamic mechanical and thermal response of the damaged structure. The damaged regions were modelled at constitutive level using a classical nonlinear elastic theory. The generation of heat in the presence of material flaws such as sliding and clapping contact at the crack interface was assumed to be generated by mechanical stresses and implemented as a constitutive model based on the classical thermoelastic theory. The FE simulations predicted the generation of the second harmonic and the temperature rise corresponding to the damaged regions represented by the nonlinear material model with good agreement with the experimental results. The proposed NUST method overcomes the main limitations of classical thermosonics by allowing detection and sizing of single and multiple barely visible impact damage in composite structures with complex geometries in a reliable and reproducible manner.

Acknowledgment

Michele Meo would acknowledge the EU FP-7 “ALAMSA” project (grant agreement number 314768), whilst Francesco Ciampa would acknowledge the EPSRC “NUSIT” project (EP/N016386/1).

References

1. DiMambro, J., et al. *Sonic infrared (IR) imaging and fluorescent penetrant inspection probability of detection (POD) comparison*. in *Review of progress in quantitative nondestructive evaluation*. 2007. AIP Publishing.
2. Kang, B.B., *Excitation method for thermosonic non-destructive testing*. 2008, Imperial College London.
3. Reifsnider, K., E.G. Henneke, and W. Stinchcomb, *The mechanics of vibrothermography.* Mechanics of nondestructive testing, 1980: p. 249-276.
4. Lu, J., et al., *Study of the effect of crack closure in sonic infrared imaging.* Nondestructive Testing and Evaluation, 2007. **22**(2-3): p. 127-135.
5. Homma, C., et al. *Study of the heat generation mechanism in acoustic thermography*. in *Quantitative Nondestructive Evaluation*. 2006. AIP Publishing.
6. Renshaw, J., et al., *The sources of heat generation in vibrothermography.* NDT & E International, 2011. **44**(8): p. 736-739.
7. Favro, L., et al., *Infrared imaging of defects heated by a sonic pulse.* Review of scientific instruments, 2000. **71**(6): p. 2418-2421.
8. Favro, L., et al., *Sonic IR imaging of cracks and delaminations.* Analytical Sciences/Supplements, 2002. **17**(0): p. s451-s453.
9. Favro, L., et al., *Sonic infrared imaging of fatigue cracks.* International journal of fatigue, 2001. **23**: p. 471-476.
10. Solodov, I. *Local defect resonance (LDR): A route to highly efficient thermosonic and nonlinear ultrasonic NDT*. in *40TH ANNUAL REVIEW OF PROGRESS IN QUANTITATIVE NONDESTRUCTIVE EVALUATION: Incorporating the 10th International Conference on Barkhausen Noise and Micromagnetic Testing*. 2014. AIP Publishing.

11. Solodov, I., et al., *A local defect resonance to enhance acoustic wave-defect interaction in ultrasonic nondestructive evaluation.* Applied Physics Letters, 2011. **99**(21): p. 211911.
12. Shuyu, L., *Equivalent circuits and directivity patterns of air-coupled ultrasonic transducers.* The Journal of the Acoustical Society of America, 2001. **109**(3): p. 949-957.
13. Fletcher, L., *Recent developments in contact conductance heat transfer.* Journal of Heat Transfer, 1988. **110**(4b): p. 1059-1070.
14. Vick, B., M.J. Furey, and C. Kajdas, *An examination of thermionic emission due to frictionally generated temperatures.* Tribology Letters, 2002. **13**(2): p. 147-153.
15. Vick, B. and M.J. Furey, *A basic theoretical study of the temperature rise in sliding contact with multiple contacts.* Tribology International, 2001. **34**(12): p. 823-829.
16. Vick, B. and M. Ozisik, *Quasi-steady-state temperature distribution in periodically contacting finite regions.* Journal of Heat Transfer, 1981. **103**(4): p. 739-744.
17. Shojaeefard, M., K. Goudarzi, and M.S. Mazidi, *Inverse heat transfer problem of thermal contact conductance estimation in periodically contacting surfaces.* Journal of Thermal Science, 2009. **18**(2): p. 150-159.
18. Ovcharenko, A., et al., *Transient thermomechanical contact of an impacting sphere on a moving flat.* Journal of Tribology, 2011. **133**(3): p. 031404.
19. Fierro, G.M., et al., *Nonlinear ultrasound modelling and validation of fatigue damage.* Journal of Sound and Vibration, 2015. **343**: p. 121-130.
20. Fierro, G.P.M. and M. Meo, *Residual fatigue life estimation using a nonlinear ultrasound modulation method.* Smart Materials and Structures, 2015. **24**(2): p. 025040.
21. Boccardi, S., et al., *Nonlinear Damage Detection and Localisation Using a Time Domain Approach.* Structural Health Monitoring 2015, 2015.
22. Fierro, G.P.M. and M. Meo, *Nonlinear imaging (NIM) of flaws in a complex composite stiffened panel using a constructive nonlinear array (CNA) technique.* Ultrasonics, 2016.
23. Cantrell, J.H., *Fundamentals and applications of nonlinear ultrasonic nondestructive evaluation.* Ultrasonic Nondestructive Evaluation: Engineering and biological material characterization, 2004: p. 363-434.
24. Ciampa, F., et al., *Detection and Modelling of Nonlinear Elastic Response in Damaged Composite Structures.* Journal of Nondestructive Evaluation, 2014. **33**(4): p. 515-521.
25. Popov, V.L., *Rigorous Treatment of Contact Problems–Hertzian Contact*, in *Contact Mechanics and Friction*. 2010, Springer. p. 55-70.
26. Basu, B. and M. Kalin, *Frictional Heating and Contact Temperature.* Tribology of Ceramics and Composites: A Materials Science Perspective, 2011: p. 60-69.
27. Pickering, S., et al., *LED optical excitation for the long pulse and lock-in thermographic techniques.* NDT & E International, 2013. **58**: p. 72-77.
28. Bremond, P. and P. Potet. *Lock-in thermography: a tool to analyze and locate thermomechanical mechanisms in materials and structures*. in *Aerospace/Defense Sensing, Simulation, and Controls*. 2001. International Society for Optics and Photonics.
29. Ibarra-Castanedo, C., et al. *Inspection of aerospace materials by pulsed thermography, lock-in thermography, and vibrothermography: a comparative study*. in *Defense and Security Symposium*. 2007. International Society for Optics and Photonics.
30. Dillenz, A., et al., *Progress in phase angle thermography.* Review of scientific instruments, 2003. **74**(1): p. 417-419.
31. Stanley, P. and W. Chan, *The application of thermoelastic stress analysis techniques to composite materials.* The Journal of Strain Analysis for Engineering Design, 1988. **23**(3): p. 137-143.
32. Fierro, G.P.M., et al. *Nonlinear thermosonics and laser vibrometry for barely visible impact damage of a composite stiffener panel*. in *SPIE Smart Structures and Materials+ Nondestructive Evaluation and Health Monitoring*. 2016. International Society for Optics and Photonics.
33. Oswald-Tranta, B. and S.M. Shepard. *Comparison of pulse phase and thermographic signal reconstruction processing methods*. in *SPIE Defense, Security, and Sensing*. 2013. International Society for Optics and Photonics.
34. Bates, D., et al., *Rapid thermal non-destructive testing of aircraft components.* Composites Part B: Engineering, 2000. **31**(3): p. 175-185.
35. Almond, D.P. and P. Patel, *Photothermal science and techniques*. Vol. 10. 1996: Springer.
36. Ciampa, F., E. Barbieri, and M. Meo, *Modelling of multiscale nonlinear interaction of elastic waves with three-dimensional cracks.* The Journal of the Acoustical Society of America, 2014. **135**(6): p. 3209-3220.
37. Hallquist, J.O., *LS-DYNA theory manual.* Livermore Software Technology Corporation (LSTC), 2006. **3**.
38. *LS-DYNA Keyword User's Manual*. 2014, LSTC: www.lstc.com.